JOURNAL OF GEOPHYSICAL RESEARCH, VOL. 105, NO. D8, PAGES 10,219–10,236, APRIL 27, 2000

Effects of snow physical parameters on spectral albedo and bidirectional reflectance of snow surface

Teruo Aoki, Tadao Aoki, Masashi Fukabori
Meteorological Research Institute, Tsukuba, Japan

Akihiro Hachikubo[1]
Institute of Low Temperature Science, Hokkaido University, Sapporo, Japan

Yoshihiro Tachibana
Research Institute of Civilization, Tokai University, Hiratsuka, Japan

Fumihiko Nishio[2]
Hokkaido University of Education, Kushiro, Japan

Abstract. Observations of spectral albedo and bidirectional reflectance in the wavelength region of $\lambda = 0.35$–2.5 μm were made together with snow pit work on a flat snowfield in eastern Hokkaido, Japan. The effects of snow impurities, density, layer structure, and grain size attained by in situ and laboratory measurements were taken into account in snow models for which spectral albedos were calculated using a multiple-scattering model for the atmosphere-snow system. Comparisons of these theoretical albedos with measured ones suggest that the snow impurities were concentrated at the snow surface by dry fallout of atmospheric aerosols. The optically equivalent snow grain size was found to be of the order of a branch width of dendrites or of a dimension of narrower portion of broken crystals. This size was smaller than both the mean grain size and the effective grain size obtained from micrographs by image processing. The observational results for the bidirectional reflection distribution function (BRDF) normalized by the radiance at the nadir showed that the anisotropic reflection was very significant in the near-infrared region, especially for $\lambda > 1.4$ μm, while the visible normalized BRDF (NBRDF) patterns were relatively flat. Comparison of this result with two kinds of theoretical NBRDFs, where one having been calculated using single-scattering parameters by Mie theory and the other using the same parameters except for Henyey-Greenstein (HG) phase function obtained from the same asymmetry factor as in the Mie theory, showed that the observed NBRDF agreed with the theoretical one using the HG phase function rather than with that using the Mie phase function, while the albedos calculated with both phase functions agreed well with each other.

1. Introduction

Snow cover is very sensitive to a climate change and has large feedback effects on the climate system. The former is because local climate affects the phase change of ice (snow) and the latter is caused by the high albedo in the visible region. The modern radiative transfer model for the snow albedo has brought us a better understanding of the optical properties of snow in the shortwave spectral region. For example, the effects of solar zenith angle, snow grain size, impurities, snowpack thickness, and incident condition on the spectral albedo were examined by *Wiscombe and Warren* [1980] and *Warren and Wiscombe* [1980] using the delta-Eddington approximation and Mie theory. *Warren* [1982] reviewed the historical development of snow albedo modelings and snow albedo observations and also described the possibility of remote sensing to estimate the snow physical parameters such as snow grain size and impurities. Satellite remote sensing of snow is important for the studies of climate change because of the large impact of the cryosphere on to the climate system. *Li* [1982] calculated the bidirectional reflection distribution function (BRDF) of snow using Mie theory and the "doubling method" and showed the anisotropic reflection property of snow. This is important for satellite remote sensing of a snow surface. *Han* [1996] developed the snow BRDF model using the discrete ordinate method and Mie theory to retrieve the surface albedo from satellite measurements in the Arctic. *Leroux et al.* [1997, 1999] developed the polarized BRDF model using the "doubling and adding" model, together with Mie theory and ray optics, and compared the theoretical values with measurements in the principal plane at $\lambda = 1.65$ μm. They demonstrated that the snow grain shape strongly affects the BRDF in the near-infrared region and that hexagonal particles rather than spherical particles give a better agreement with measurements. *Leroux and Fily* [1998] developed the BRDF model, including the

[1]Now at Kitami Institute of Technology, Kitami, Japan.
[2]Now at Center for Environmental Remote Sensing, Chiba University, Chiba, Japan.

Copyright 2000 by the American Geophysical Union.

Paper number 1999JD901122.
0148-0227/00/1999JD901122$09.00

effect of sastrugi with regularly spaced identical rectangular protrusions. *Aoki et al.* [1999] examined the atmospheric effects, such as atmospheric molecules, absorptive gases, aerosols, and clouds, on the spectral and spectrally integrated snow albedos at the surface and at the top of the atmosphere. Thus the snow albedo models have been incorporated into the atmosphere-snow system and have become applicable to the remote sensing of a snow surface with BRDF properties being taken into consideration.

To study the optical properties of snow, it is necessary to make spectral measurements of snow as well as to apply theoretical approaches. *Liljequist* [1956] has observed the albedos in four visible bands using a photoelectric cell and color filters and reported that the maximum albedo was 0.97 in the band of $\lambda = 0.52$ μm. Measurements of albedo with higher spectral resolution have been made by *Grenfell and Maykut* [1977] for $\lambda = 0.4$–1.0 μm using a prism spectrometer on ice and snow in the Arctic sea. They demonstrated an effect of the aging of snow on albedo and that the maximum albedo of dry snow was in the range of $\lambda = 0.4$–0.6 μm. *Kuhn and Siogas* [1978] reported results on spectral albedo for a wider spectral range of $\lambda = 0.39$–1.55 μm for different types of snow in the Antarctic using a spectrometer. The visible albedos observed by *Grenfell and Maykut* [1977] and *Kuhn and Siogas* [1978] were too low compared to the theoretically predicted ones for pure snow in the polar region. *O'Brien and Koh* [1981] observed the shallow snow reflectance in the six near-infrared bands from $\lambda = 0.81$ to 1.80 μm using a radiometer equipped with bandpass filters. They determined the snow grain size through image processing for replicated snow samples. Since this was actually the size of snow aggregates, the theoretically predicted grain size of new snow, as estimated from the values of the near-infrared reflectance, was much smaller than that estimated on the basis of image processing. Spectral albedo measurements for a wide solar spectrum range ($\lambda = 0.38$–2.45 μm) have been made by *Grenfell et al.* [1981] on a snowfield in the Cascade Mountains in the United States using the spectrometer described by *Grenfell* [1981]. They examined the effects of snow grain size and impurities on the spectral albedo for a wide range of snow lifetime from new snow to granular snow. *Grenfell and Perovich* [1984] observed spectral albedos for different types of sea ice in the Arctic sea. They concluded that the variation in albedos is due primarily to differences in vapor bubble density, crystal structure, and free water content of the upper layers of the ice. *Warren et al.* [1986] observed the spectral albedo for $\lambda = 0.3$–2.5 μm in Antarctica using two kinds of spectrometers, including the type described by *Grenfell* [1981], and obtained a high value (close to unity) at visible wavelengths, as was theoretically predicted for pure snow. However, in the near-infrared region the observed albedos were higher than those predicted for homogeneous snow, suggesting that the snow surface was covered by smaller snow grains. *Grenfell et al.* [1994] observed spectral albedos on an Antarctic snowfield under cloudy conditions which showed a good agreement with the theoretical ones calculated by means of a two-layer snow model. On the other hand, some discrepancies remained at the near-infrared wavelengths under a clear sky. The reason for these discrepancies was not yet realized although they quoted the following possibilities: underestimation of snow grain size, inaccurate correction of the instrument, and a fault in the model. *Sergent et al.* [1998] showed the dependency of spectral hemispherical-directional reflectance on four types of snow in the region of $\lambda = 0.9$–1.45 μm in a cold laboratory. *Aoki et al.* [1998] examined the spectral albedos for $\lambda = 0.35$–2.5 μm using a grating spectrometer on a snowfield at Barrow, Alaska, under a cloudy condition, and demonstrated that the optically equivalent grain size (although they originally used "optically effective grain size," we will use this term to avoid any confusion with "effective radius" used for the size distribution) is of the order of the branch width of dendrites for new snow.

Most measurements mentioned above were made under cloudy conditions. However, it is necessary to examine the optical properties of snow under a clear sky in preparation for the satellite remote sensing of snow using an optical sensor. The measurement of spectral albedos under clear conditions is very difficult due to the following three reasons [*Warren et al.*, 1986]: The incident radiation is primarily a direct solar beam, while the upward radiation is diffuse. (1) A little deviation of the level setting of the instrument causes an error. (2) The deviation from the so-called "cosine property" of the incident angular sensitivity of the instrument must be corrected precisely. This correction must be applied to the diffuse component as well as to the direct component, where the correction factor generally depends on the wavelength. (3) Even a gentle slope of the snow surface can cause the snow albedo to be computed erroneously if not accounted for. In general, an optically thin cosine collector, which measures transmitted light, has an incident angle dependence that deviates much from the perfect cosine property. Although this deviation would become small for an optically thick cosine collector, the transmittance becomes degraded as the thickness increases. This causes a poor signal to noise (SNR) ratio. Therefore for the accurate spectral albedo measurement under a clear sky, the following are required: (1) introduction of a measurement technique with fewer systematic errors, (2) appropriate correction on the measured spectrum, and (3) careful selection of the snow surface on the observation site. We have obtained the spectral albedo under a clear sky by means of an observation system using a white reference standard together with correction for errors due to the observation system. These albedos were compared with the theoretically calculated ones, and the effects of snow physical parameters on the spectral albedo were investigated.

BRDF observation of a snow surface is very important for satellite remote sensing of a snow surface or of the atmosphere above a snow surface because of the anisotropic feature of snow reflectance. The early BRDF observations of snow surfaces were made for broad spectral regions on the snowfield [*Salomonson and Marlatt*, 1968; *Kuhn*, 1974; *Dirmhirn and Eaton*, 1975] and in the cold laboratory [*O'Brien and Munis*, 1975; *O'Brien*, 1977]. These studies showed the anisotropic reflection properties of snow. *Kuhn and Siogas* [1978] observed the monochromatic BRDF at $\lambda = 0.45$ μm at the South Pole in Antarctica and reported the effect of sastrugi. *Taylor and Stowe* [1984a, b] demonstrated the basic features of BRDF at the top of the atmosphere for snow, cloud, land, and ocean with Nimbus-7 ERB data. *Kuhn* [1985] examined the BRDF at $\lambda = 0.45$, 0.514, 0.75, and 1.0 μm under specific geometric conditions at several Antarctic sites and an alpine snow surface. *Steffen* [1987] demonstrated the effects of snow grain size and snow type on BRDF properties from measurements using an instrument with a bandpass filter of $\lambda = 0.4$–0.5 μm in the Tienshan Mountains of China. *Brandt et al.* [1991] advanced Kuhn's work and showed the effects of the direction of sastrugi on the BRDF at $\lambda = 0.9$ μm as obtained from measurements

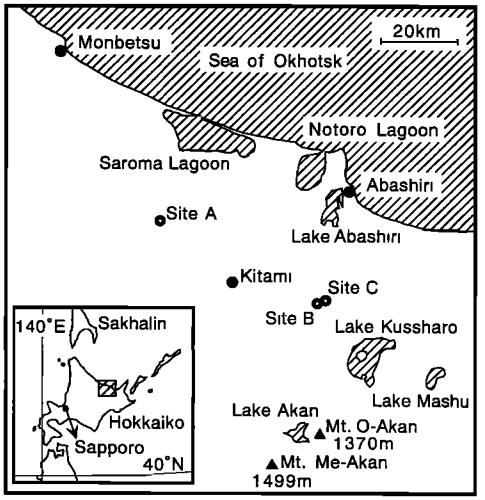

Figure 1. Map showing the locations of observation sites in eastern Hokkaido, Japan. The Sea of Okhotsk was mostly covered by sea ice during the observation period. The prevailing wind at the time of snowfall was northwestern.

at the South Pole in Antarctica taking advantage of the constant solar zenith angle over the course of a day. *Carlson and Arakelian* [1993] reported that the most anisotropic reflection in the principal plane was observed at $\lambda = 2.0$ μm as determined from reflection data from 0.5 to 2.3 μm at Vostok in Antarctica. *Grenfell et al.* [1994] showed the BRDF pattern averaged over all Sun-sastrugi azimuth angles at $\lambda = 0.9$ μm at the South Pole in Antarctica. *Steffen* [1997] made the same observation as *Steffen* [1987] in Greenland and showed the BRDF patterns for several geometric conditions. *Warren et al.* [1998] studied the effect of surface roughness on the BRDF at $\lambda = 0.6$, 0.66, and 0.9 μm observed at the South Pole in Antarctica from the point of view of satellite remote sensing. Thus BRDF observations have been made for some extent of snow conditions, wavelengths, and geometry. However, since natural snow surface conditions show wide variations, BRDF observations are required under various snow conditions with narrow spectral resolution in a wider spectral range and under various geometric conditions. On the other hand, it may be said that more theoretical studies on BRDF of snow are still required. For example, the BRDF is very sensitive to snow grain shape in the near-infrared region. Thus we have to investigate what kind of a phase function is suitable for BRDF calculation. It is not clear if the hexagonal ice plate shown by *Leroux et al.* [1999] is applicable to all snow type. For such subjects it is necessary to compare the measured BRDFs of snow under various conditions with the theoretically calculated ones.

The first objective of this study is to investigate the effects of snow physical parameters (snow grain size, impurities, and layer structure) on spectral albedo under clear conditions using the spectral data, snow pit work data, and a radiative transfer model. The second objective is to investigate the BRDF properties of snow and obtain the basic knowledge required to develop an accurate BRDF model. This work is linked with the satellite remote sensing program, which is to retrieve snow grain size and snow impurities using data obtained by means of an optical sensor GLI (global imager) mounted on the Japanese satellite ADEOS II (Advanced Earth Observing Satellite II), which will be launched in 2000 [*Nakajima et al.*, 1998]. Therefore the BRDF analysis was done for six selected wavelengths in the visible and the near-infrared regions from among the 36 channels of GLI.

2. Observation Conditions

Spectral albedo observations with snow pit work were made on February 22–25, 1998, at three sites on a snowfield around Kitami in eastern Hokkaido, Japan (Figure 1, Table 1). These observation sites were seasonally snow covered flat farms, where there were no shadows caused by surface roughness, although slight undulation was seen. The spectral albedo data were selected under the conditions where the solar zenith angle was close to 53° which was the value at local solar noon, and the snow surface was illuminated by a direct solar beam. The sky conditions were clear except on February 22 as shown in Table 1. A new snowfall was observed on February 20 with a depth of about 10 cm and on February 21 with a depth of less than 1 cm. Snow conditions at the snow surface changed from new snow to faceted crystals or granular snow during the observation period, as shown in Figure 2, and those in the lower part were depth hoar throughout this period. Snow grain size (radius) was estimated using a handheld lens together with micrographs to provide the size distribution. In situ measurements with a handheld lens gave two kinds of dimensions of grain size: one was one-half the length of the major axis of crystals or dendrites (r_1), and the other was one-half the branch width of dendrites or one-half the dimension of the narrower portion of broken crystals (r_2). Figure 3 shows micrographs for the surface snow (Figures 3a–3d) from February 22 to 25 and those for 5- and 20-cm depths on February 23 (Figures 3e–3f). These micrographs together with other pictures were used to estimate the size distribution of circle-equivalent radius for the projected grains by means of the image-processing software "Image Hyper II" made by Inter Quest Inc. (Japan). The procedure of this image processing was as follows: The digitized image of each micrograph of snow grains was converted to binary tone with an adequate threshold level. Highly aggregated grains were masked automatically. For the remaining grains the projected area was directly measured for independent grains. In the case of a few grains attached to each other they were separated into independent grains by estimating the area of overlapping between individual

Table 1. Locations and Conditions of Observation of Snow Albedo

1998	Site	Latitude/Longitude	Height	Local Time	θ_0	Sky Condition
Feb. 22	A	43°56′20″N/143°39′25″E	105 m	1126–1141	54.2°–54.3°	5/10 Cu and 1/10 Ac
Feb. 23	B	43°45′33″N/144°10′26″E	57 m	1014–1015	56.8°–56.9°	1/10 Cu
Feb. 24	C	43°45′55″N/144°11′18″E	75 m	1223–1225	54.4°–54.5°	clear
Feb. 25	B	43°45′33″N/144°10′26″E	57 m	1034–1036	54.7°–54.8°	clear

Value of θ_0 means the solar zenith angle.

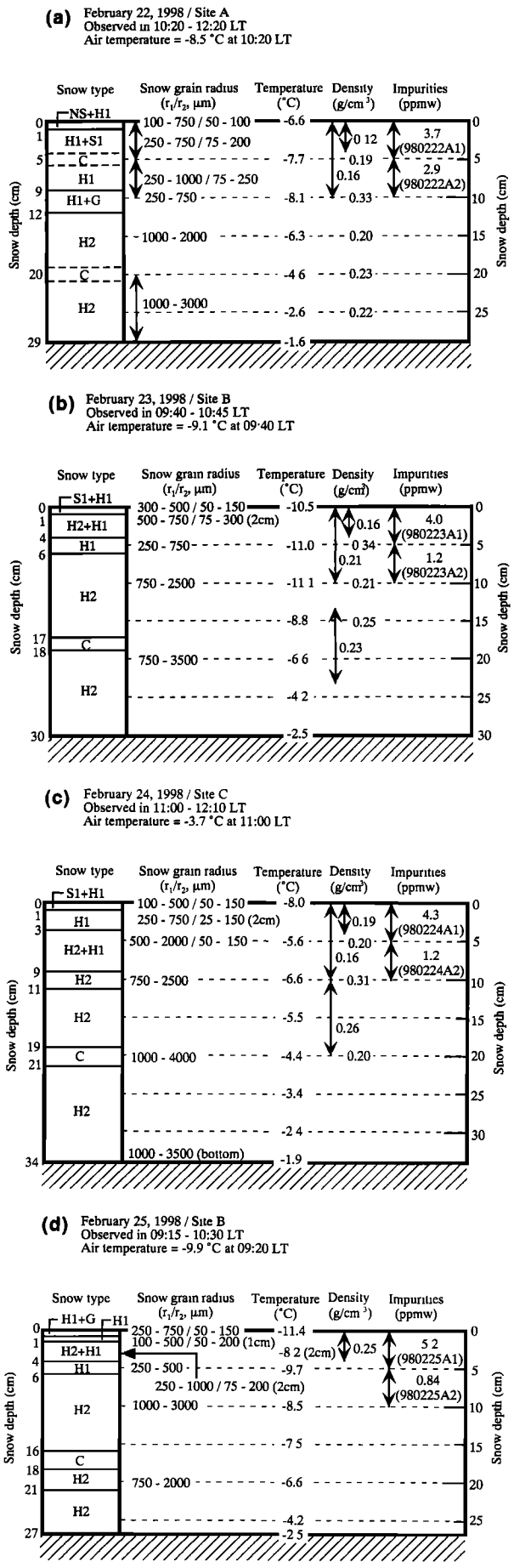

grains by means of a sphere-separating algorithm. The circle-equivalent radius was calculated from the projected area, and the mean radius ($\bar{r}_{\text{image}}$) and the effective radius ($r^{\text{eff}}_{\text{image}}$, area-weighted mean radius [after *Hansen and Travis*, 1974]) were obtained. *Grenfell et al.* [1994] and *Grenfell and Warren* [1999] argued that spheres of equal volume-to-area (V/A) ratio are more appropriate as the optically equivalent snow grain size. Unfortunately, we could not estimate the radius of the equal-V/A sphere accurately for irregular snow grains on our micrographs. The optically equivalent snow grain size will be discussed using the roughly estimated radius of the equal-V/A sphere in section 6.3. The resultant size distribution is shown in Figure 4. The size distribution of the snow grain radius was wider on later days than on early days, and the mean radius $\bar{r}_{\text{image}}$ was also larger on later days. The values of $\bar{r}_{\text{image}}$ were closer to r_2 than r_1 at the snow surface in Figure 2 and were close to the highest values in the range of r_2. From Figures 2 to 4 we see that the surface grain size increased with the lapse of time, and it was generally smaller at the surface than in the deeper layers. These facts are due mainly to the formation of faceted crystals or depth hoar. The snow density around the surface was lowest on February 22 and became higher on later days. The snow impurities (water-dissolved solid particles in the snowpack) were filtered within a day using Nuclepore filters with a diameter of 25 mm and the pore size of 0.2 μm, after melting the snow samples of the surface layer (0–5 cm) and of the subsurface layer (5–10 cm). The concentrations of impurities were estimated by direct measurements of the weight of the Nuclepore filters, before and after filtering, using a balance.

3. Instrumentation

The spectral albedo was observed using a grating spectrometer, "FieldSpec FR," made by ASD Inc. (United States). The scanning spectral range of this instrument was 0.35–2.5 μm with the spectral resolution of 3 nm for λ = 0.35–1.0 μm and 10 nm for λ = 1.0–2.5 μm. The scanning time was 1 s with a sampling interval of 1 nm for the full spectral range. The detectors were one-dimensional Si photodiode CCDs for λ = 0.35–1.0 μm and two different types of InGaAs photodiodes for λ = 1.0–1.8 μm and λ = 1.8–2.5 μm. To obtain the albedo, measurements of downward and upward fluxes were necessary. However, it was very difficult to measure the downward flux accurately under clear conditions, as stated by *Warren et al.* [1986]. Thus we made an albedo observation system (Figure 5) using a white reference standard (WRS) of $BaSO_4$ "SRT-99" made by Labsphere Inc. (United States). The WRS was attached horizontally to the tip of a pipe (black part in Figure 5,

Figure 2. (opposite) Vertical profiles of snow parameters obtained from snow pit work from (a–d) February 22 to 25, 1998. Snow types are indicated as NS for new snow, H1 for faceted crystals, H2 for depth hoar, S1 for fine-grained old snow, C for crust, and G for granular snow. Snow grain sizes were measured with ~10-μm resolution using a handheld lens for two kinds of dimensions, where one-half the length of major axis of crystals or dendrites (r_1), and the other is one-half the branch width of dendrites or one-half the dimension of the narrower portion of broken crystals (r_2). Snow impurities were collected on the Nuclepore filters and the concentration was estimated by means of a balance. The snow sample name is indicated in parentheses below the concentration of impurities.

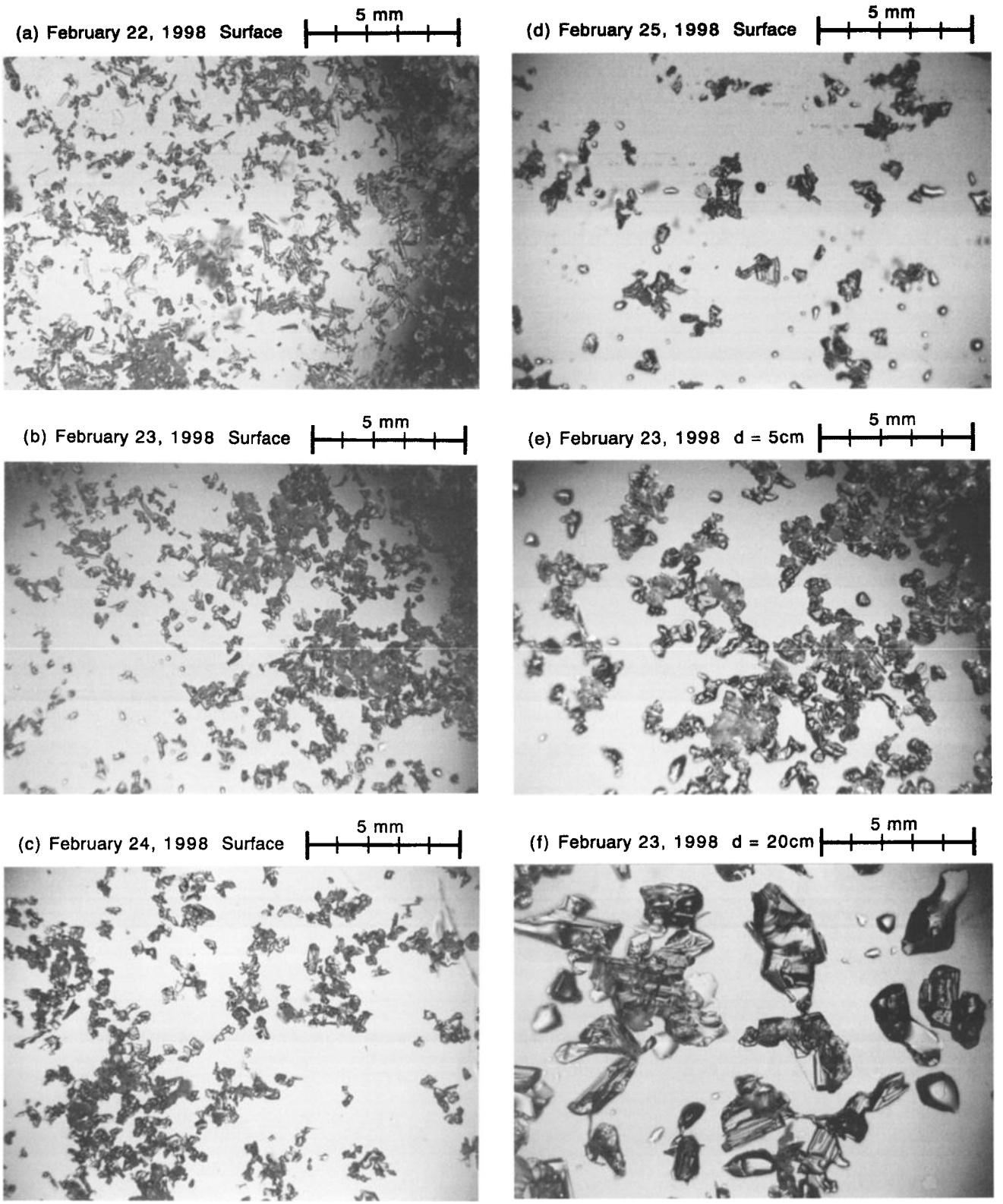

Figure 3. Micrographs of snow grains (a–d) for the surface from February 22 to 25, 1998 and (e–f) for 5-cm and 20-cm depths on February 23, 1998.

bottom) stretching from the mount set on the top of a tripod. The length of the pipe was 0.9 m. The downward flux was observed by directing the optical fiber tip of the spectrometer downward to the upper surface of WRS. In the case of the upward flux observation an arm holding the optical fiber tip (hatched parts in Figure 5, bottom (hereinafter referred to as the "optical fiber arm")) was turned by 180° around the pipe. The optical fiber had a conical field of view (FOV) subtending

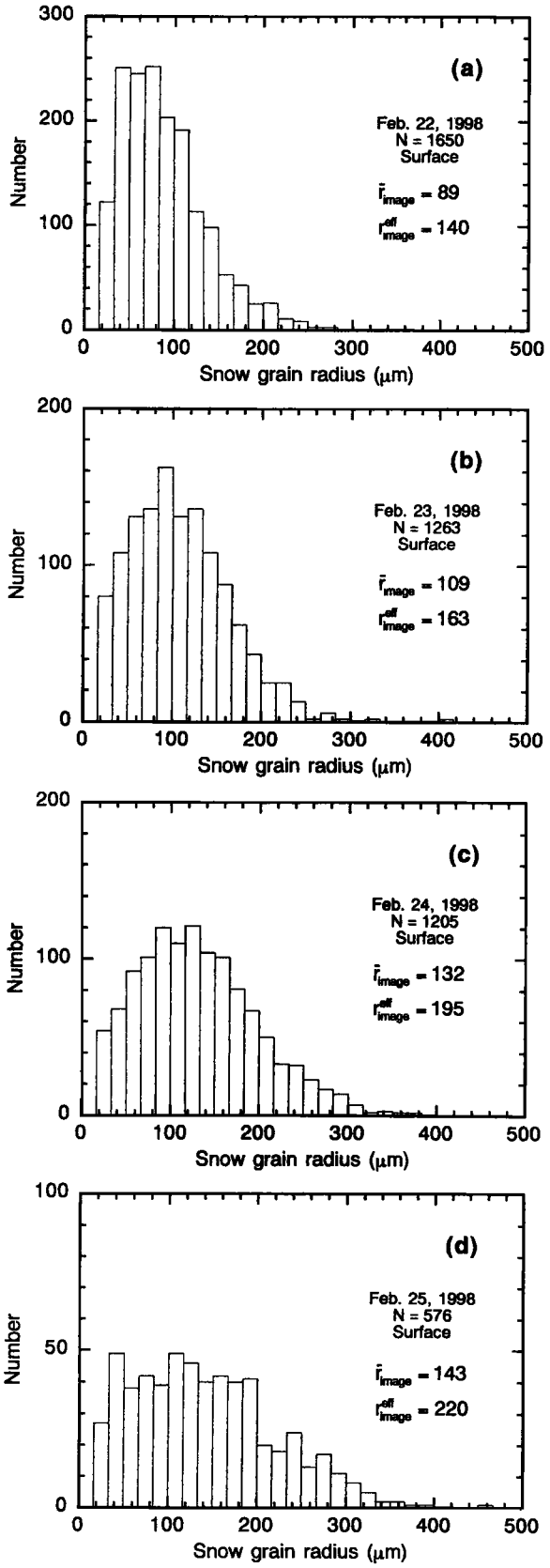

Figure 4. Size distributions of sphere-equivalent radius of snow grains at the surface obtained by image processing from (a–d) February 22 to 25, 1998. The values $\bar{r}_{image}$ and r^{eff}_{image} are the mean radius and the effective radius, respectively, and N is the total number of processed snow grains. The highly aggregated grains on the micrographs were excluded in image processing.

a full angle of ~25°. The distance of WRS from the snow surface was about 0.3 m.

This method has some advantages, as follows: (1) the level of WRS can be set accurately by means of a spirit level and does not change throughout the measurements; (2) it is not necessary to know the absolute reflectance of WRS for albedo measurements; and (3) the cosine property of reflection is generally better than that of a cosine collector. The deviation from the perfect cosine behavior of the cosine collector used by *Grenfell et al.* [1994] was, at maximum, 10% at the incident angle of 60° and 40% for 80°, and its wavelength dependence was also very large. In our case, it was about 8% at the incident angle of 60° and about 20% for 80° with slight spectral dependence (Figure 6a). Our system, however, underestimated the fluxes due to the shading by the optical fiber arm. These effects were corrected as will be shown in the next section. The spectral albedo for one snow surface was calculated by averaging

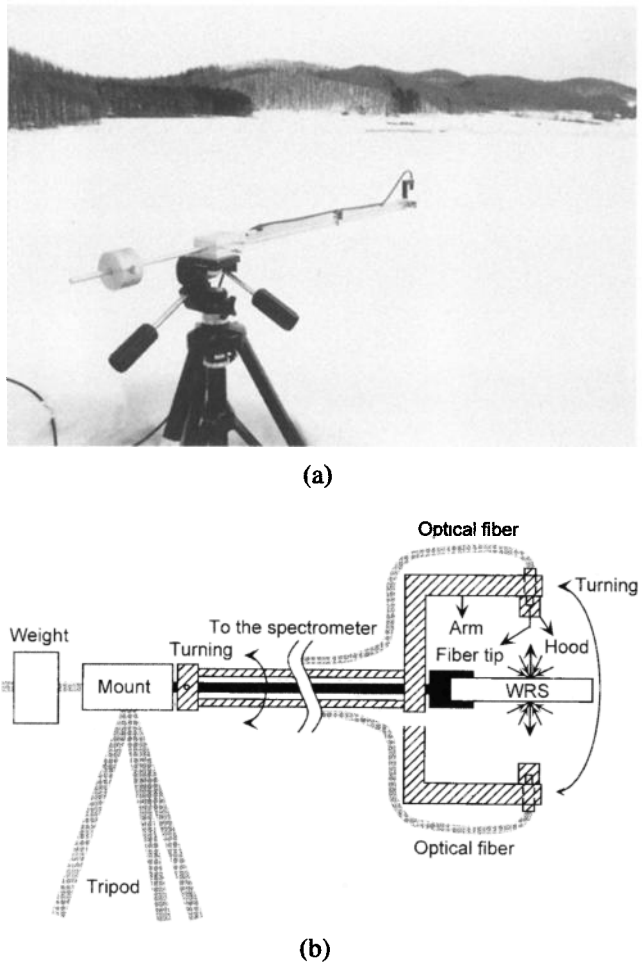

Figure 5. Albedo observation system: (top) photograph of the observational setup, and (bottom) schematic diagram of the setup for downward and upward flux observations. The downward flux was observed by directing the optical fiber tip of the spectrometer downward to the upper surface of the white reference standard (WRS) which was attached horizontally to the edge of a pipe (black part) with a length of 0.9 m stretching from the mount on a tripod. In the case of the upward flux observation, an arm holding the optical fiber tip (hatched parts) turned by 180° around the pipe. The distance of WRS from the snow surface was about 0.3 m.

five spectral albedos obtained from five pairs of measurements for downward and upward (snow reflected) solar fluxes. In general, it takes less than a few minutes to measure these quantities under clear conditions. However, on February 22 it took 16 min due to the presence of broken clouds. The standard deviation for these five observed albedos was also calculated to check the data quality.

4. Corrections for Radiant Flux and Albedo

Two kinds of effects should have been taken into account to obtain the radiant flux with our instrument: one was the deviation from the cosine property of WRS and the other was the influence of shading by the optical fiber arm. The former was calibrated in a laboratory (Figure 6a), where WRS was illuminated from different incident angles by a direct solar (parallel) beam led by the mirror of a heliostat. In this calibration there were no data for the incident angles less than 20° due to the shadow of the optical fiber tip on WRS. Since the deviation from the cosine property would be very small at small incident angles, we assumed that the reflectance of WRS for the incident angles less than 20° followed the cosine property. Figure 6a shows that the spectral dependence of the reflection property of WRS was very small. In the atmospheric absorption bands the SNRs of measured spectra in this calibration were not very good due to the use of direct solar radiation. Thus we used the calibration curve at $\lambda = 0.52$ μm with high SNR for all wavelengths. The influence of shading by the optical fiber arm is also shown in Figure 6a, where the azimuthally integrated shading fraction is plotted for each incident angle viewed from the center of the field of view of the optical fiber on WRS.

Figure 6a shows that our observation system would have underestimated the radiant flux due to the two factors mentioned above. We now define a factor $f(\theta, \phi)$ as the ratio of the observed value to the true one for the radiant flux coming only from the incident angle θ and the azimuth angle ϕ. For the incidence of isotropic diffuse radiation the ratio of the observed radiant flux to the true one f_{diff} is given by

$$f_{\mathrm{diff}} = 2 \int_0^{\pi/2} \bar{f}(\theta) \sin\theta \cos\theta \, d\theta, \qquad (1)$$

where $\bar{f}(\theta)$ is the azimuthally integrated value of $f(\theta, \phi)$ and is given by

$$\bar{f}(\theta) = \frac{1}{2\pi} \int_0^{2\pi} f(\theta, \phi) \, d\phi. \qquad (2)$$

For the direct solar beam the ratio of observed radiant flux to the true one is expressed by $f_{\mathrm{dir}}(\theta, \phi) = f(\theta = \theta_0, \phi = \phi_0)$, where θ_0 and ϕ_0 are the solar zenith and solar azimuth angles, respectively. Although the upward flux and the diffuse component in the downward flux are anisotropic in the strict sense, we assumed these fluxes are isotropic here. In our system the ordinate in Figure 6a corresponds to $\bar{f}(\theta)$ for WRS and $1 - \bar{f}(\theta)$ for shading by the optical fiber arm. In the case of WRS the ϕ dependence of $f(\theta, \phi)$ is so small that we assumed $\bar{f}(\theta) = f(\theta)$. For the direct solar beam we also assumed $f_{\mathrm{dir}}^{\mathrm{WRS}}(\theta_0, \phi_0) = f(\theta_0)$. Putting the data of Figure 6a into (1), $f_{\mathrm{diff}}^{\mathrm{WRS}} = 0.946$ and $f_{\mathrm{diff}}^{\mathrm{arm}} = 0.934$ are obtained, respectively, for WRS and the shading by the optical fiber arm. The correction

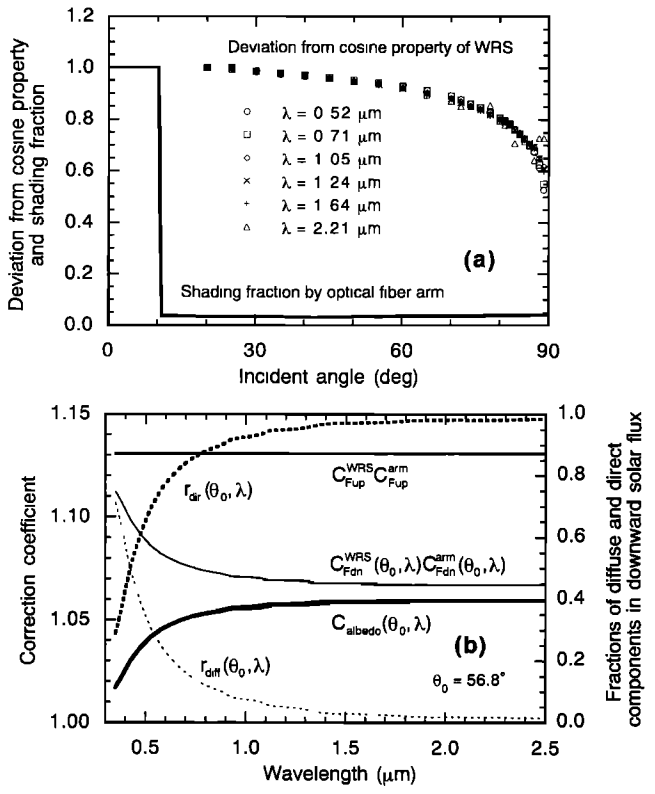

Figure 6. (a) Deviation from the perfect cosine property in the incident angle dependence of the reflectance of WRS (shown by characters) and the azimuthally integrated shading fraction by the optical fiber arm for each angle of incidence viewed from the center of the field of view of the optical fiber on WRS (solid line). The underestimate of radiant flux due to the imperfect cosine property of WRS was 5.36% for complete diffuse illumination and 6.19% for direct solar beam at $\theta_0 = 56.8°$. The total shading fraction by the optical fiber arm was 6.56% for complete diffuse illumination. (b) Fractions of the diffuse component ($r_{\mathrm{diff}}(\theta_0, \lambda)$, thin dashed line) and the direct component ($r_{\mathrm{dir}}(\theta_0, \lambda)$, thick dashed line) in downward solar flux theoretically calculated for $\theta_0 = 56.8°$, and correction coefficients for upward solar flux ($C_{\mathrm{Fup}}^{\mathrm{WRS}} C_{\mathrm{Fup}}^{\mathrm{arm}}$, middle solid line), downward solar flux ($C_{\mathrm{Fdn}}^{\mathrm{WRS}}(\theta_0, \lambda) C_{\mathrm{Fdn}}^{\mathrm{arm}}(\theta_0, \lambda)$, thin solid line), and albedo ($C_{\mathrm{albedo}}(\theta_0, \lambda)$, thick solid line) on February 23, 1998.

of WRS should be made for both the direct and the diffuse components in downward solar flux, and the correction coefficient $C_{\mathrm{Fdn}}^{\mathrm{WRS}}(\theta_0, \lambda)$ for downward flux is given by

$$C_{\mathrm{Fdn}}^{\mathrm{WRS}}(\theta_0, \lambda) = \frac{r_{\mathrm{dir}}(\theta_0, \lambda)}{f_{\mathrm{dir}}^{\mathrm{WRS}}(\theta_0)} + \frac{r_{\mathrm{diff}}(\theta_0, \lambda)}{f_{\mathrm{diff}}^{\mathrm{WRS}}}, \qquad (3)$$

where $f_{\mathrm{dir}}^{\mathrm{WRS}}(\theta_0)$ is obtained from the data for WRS in Figure 6a, and $r_{\mathrm{dir}}(\theta_0, \lambda)$ and $r_{\mathrm{diff}}(\theta_0, \lambda)$ are the fractions of direct and diffuse components in downward total flux (i.e., $r_{\mathrm{diff}} = 1 - r_{\mathrm{dir}}$), respectively. We calculated these fractions using the radiative transfer model for the atmosphere-snow system, which will be described in section 5. The calculated values of r_{dir} and r_{diff} for February 23, 1998 ($\theta_0 = 56.8°$) are shown on the right-hand ordinate in Figure 6b. Since the optical fiber arm held the fiber tip on the opposite side from the Sun and did not affect the measurement of direct solar radiation for $\theta_0 > 20°$, only the diffuse component should be corrected in the down-

ward solar flux, and the correction coefficient $C^{arm}_{Fdn}(\theta_0, \lambda)$ is given by

$$C^{arm}_{Fdn}(\theta_0, \lambda) = \frac{r_{diff}(\theta_0, \lambda)}{f^{arm}_{diff}}. \quad (4)$$

For upward solar flux the correction coefficients C^{WRS}_{Fup} for WRS and C^{arm}_{Fup} for the optical fiber arm are simply given by

$$C^{WRS}_{Fup} = \frac{1}{f^{WRS}_{diff}}, \quad (5)$$

$$C^{arm}_{Fup} = \frac{1}{f^{arm}_{diff}}. \quad (6)$$

The total correction coefficients for downward and upward solar fluxes are given by $C^{WRS}_{Fdn}(\theta_0, \lambda)C^{arm}_{Fdn}(\theta_0, \lambda)$ and $C^{WRS}_{Fup}C^{arm}_{Fup}$, respectively, and thus the resultant net correction for albedo is expressed by

$$C_{albedo}(\theta_0, \lambda) = \frac{C^{WRS}_{Fup}C^{arm}_{Fup}}{C^{WRS}_{Fdn}(\theta_0, \lambda)C^{arm}_{Fdn}(\theta_0, \lambda)}. \quad (7)$$

The correction coefficients for February 23 are shown on the left-hand ordinate in Figure 6b. In our system the correction coefficient for upward flux was larger than that for downward flux. However, for the calculation of albedo they canceled out each other in part, and the resultant net correction was less than 1.06.

5. Radiative Transfer Model

5.1. Basic Features of the Radiative Transfer Model

A multiple-scattering radiative transfer model for the atmosphere-snow system was used for calculating the fractions of direct and diffuse components in downward solar flux mentioned in the previous section and was used to compare the observed spectral albedo of snow with the theoretical one. In the model, snow grains were assumed to be mutually independent ice particles, and radiative transfer was treated in the same manner as in the usual multiple-scattering model in an atmosphere containing aerosols or cloud particles. Radiative transfer calculations were based on Mie theory for single scattering and the doubling and adding method for multiple scattering omitting polarization. The details of this model have been described by *Aoki et al.* [1999]. However, in the present study, the imaginary part of the complex index of refraction of ice revised by *Kou et al.* [1993] was used only for $\lambda \geq 1.45$ μm. In the calculation for the fractions of direct and diffuse components in downward solar flux, we assumed the model atmosphere of midlatitude winter [*Anderson et al.*, 1986] together with the rural model for aerosols [*Air Force Geophysics Laboratory (AFGL)*, 1985]. The aerosol optical depth was assumed to be 0.1 at $\lambda = 0.5$ μm from the Sun photometer measurements in winter from 1993 to 1998 [*Japan Meteorological Agency (JMA)*, 1999; JMA, unpublished, 1999] at Ryori Station (39°02′N, 141°50′E, 230 m), which was a background monitoring station nearest to our observation sites. For the calculation of spectral albedo for the comparison with the observed one, a simplified model atmosphere was employed in the radiative transfer model for the atmosphere-snow system. This was because the effects of gaseous absorption and aerosols with an optical depth of 0.1 on the spectral snow albedo were both small enough for $\theta_0 \leq 63.1°$ [*Aoki et al.*, 1999], at which our observation was made, so we assumed the aerosol-free Rayleigh atmosphere without gaseous absorption.

The BRDFs of the snow surface were calculated at six wavelengths (0.52, 0.71, 1.05, 1.24, 1.64, and 2.21 μm) selected from among the GLI 36 channels using the radiance model for the atmosphere-snow system extended from the flux model mentioned above. Since there is no strong gaseous absorption at the wavelengths concerned, we assumed the Rayleigh atmosphere, including aerosols mentioned above without the gaseous absorption for BRDF calculation. The adopted definition of BRDF is the commonly used one given by

$$BRDF_\lambda(\theta_v, \theta_0, \Delta\phi) = \frac{I_\lambda(\theta_v, \theta_0, \Delta\phi)}{F_\lambda(\theta_0)}, \quad (8)$$

where θ_v and θ_0 are the viewing angle and the incident zenith angle of direct solar beam, respectively; $\Delta\phi$ is the relative azimuth angle of the viewing direction from the solar direction; $I_\lambda(\theta_v, \theta_0, \Delta\phi)$ is the reflected radiance from the snow surface; and $F_\lambda(\theta_0)$ is the downward solar flux.

5.2. Optical Characteristics of Snow Impurities

Warren and Wiscombe [1980] demonstrated that snow impurities reduce the spectral snow albedo in the visible region and have no effect on spectral albedo for $\lambda > 0.9$ μm where ice itself becomes a strong absorber. The reduction of visible albedo is different depending on the mixing type, such as external and internal mixtures [*Chýlek et al.*, 1983]. To examine the mixing type, we took scanning electron microscope (SEM) photographs of snow impurities collected on the Nuclepore filters (Figure 7). Since these particles comprise a large variety in terms of size and shape, it is considered that a large proportion of them were materials of soil origin. A small amount of spherical particles (maybe minerals) or particles that appeared to be coagulated (maybe soot) were also recognized. These morphological characteristics suggest that they were anthropogenic aerosols produced by fuel burning. The concentration of these impurities at the snow surface increased with time, as shown in Figure 2. In view of these observations, most of the snow impurities were considered to be contained in snow as an external mixture.

When the effect of snow impurities on spectral albedo is simulated as an external mixture, it is necessary to calculate the single-scattering parameters for the particles of impurities. For such calculation the Mie theory is used, where the particle size distribution and the complex refractive index of impurities are required. To obtain the size distribution of the impurities from the SEM pictures, a sample with a low concentration of impurities on the Nuclepore filter was required. However, since some particles in our collected samples were overlapping each other on the Nuclepore filter, it was difficult to estimate the size distribution accurately. We determined only the mean particle radius as 1.0 μm from the SEM pictures, including Figure 7, and assumed a standard size distribution of the gamma type [*Hansen*, 1971] with an effective variance of 0.125. The imaginary part of the refractive index of the impurities is the most important factor that affects albedo reduction, and it is obtained from the absorption coefficient by the following relation:

$$m_{im}(\lambda) = \frac{\lambda\beta_a(\lambda)}{4\pi}, \quad (9)$$

where $m_{im}(\lambda)$ is the imaginary part of the refractive index and $\beta_a(\lambda)$ is the volume absorption coefficient. For measurements

of the absorption coefficient, many techniques have been developed [*Clarke*, 1982]. *Lindberg and Laude* [1974] measured $\beta_a(\lambda)$ from the diffuse reflectance of impurities mixed with the $BaSO_4$ diluting agent based on the Kubelka and Munk theory. Since this technique requires a sample of several milligrams and it makes the sample unsuitable for the use in SEM analysis after the measurement, this method was not applied to our samples. *Clarke* [1982] developed the integrating sandwich (IS) method in which a Nuclepore filter loaded with the impurities sandwiched between two high-reflectance diffusing wafers, and the total transmittance is measured. This method can be applied only to well-scattered samples and was not applicable to our samples due to the overlapping of particles on the filter. We employed the integrating plate (IP) method [*Lin et al.*, 1973; *Clarke*, 1982] to measure $\beta_a(\lambda)$ from our samples collected on the Nuclepore filters. In this method the diffuse transmittance of the Nuclepore filter loaded with the sample is measured. Since our sample was somewhat thick for this method, multiple scattering by particles in the sample might have caused overestimation of $\beta_a(\lambda)$. Furthermore, according to *Clarke* [1982] the value of $\beta_a(\lambda)$ obtained by the IP method could be overestimated due to the internal reflection of the Nuclepore filter and multiple reflection between the Nuclepore filter and the surface of the substrate (opal glass diffuser). To eliminate the third influence, we used an integrating sphere as a light source and made the illumination diffuse without using an opal glass diffuser. The value of $\beta_a(\lambda)$ is obtained from the spectral measurement for net transmittance of impurities $T(\lambda)$ as

$$\beta_a(\lambda) = -\frac{1}{d} \ln (T(\lambda)), \tag{10}$$

where d is the depth of the layer of impurities on the Nuclepore filter. The value of d is estimated from the weight w of the impurities, their density ρ_t and the filtration area S_f (= 2.27 cm^2) of the Nuclepore filter by the relation

$$d = \frac{w}{\rho_t S_f}. \tag{11}$$

We used the values measured with balance for w as mentioned in section 2 and took the typical value of soil 2.0 g/cm^3 for ρ_t [*Japanese National Astronomical Observatory*, 1999]. We thereby obtained the imaginary part of the refractive index of snow impurities, $m_{im}(\lambda)$, as shown on the left-hand scale in Figure 8 for sample 980223A1. The values of $m_{im}(\lambda)$ for all samples from February 22 to 25 lie in the range $1.4 \times 10^{-2} \sim 2.7 \times 10^{-2}$ at $\lambda = 0.5$ μm and $4.1 \times 10^{-2} \sim 7.2 \times 10^{-2}$ at $\lambda = 2.0$ μm. *Warren and Wiscombe* [1980] reviewed the measurements of snow impurities and showed that the values of the imaginary part of the refractive index in the visible region are of the order of 10^{-2}. However, those for pure substances generally vary widely over a large range of wavelength and are different from each other [*Bohren and Huffman*, 1983]. Figure 8 also shows the values of $m_{im}(\lambda)$ for soot [*AFGL*, 1985], dust-like aerosol [*AFGL*, 1985], and ice [*Warren*, 1984; *Kou et al.*, 1993] on the same scale just for comparison. Our estimated values of $m_{im}(\lambda)$ were somewhat higher than the values for

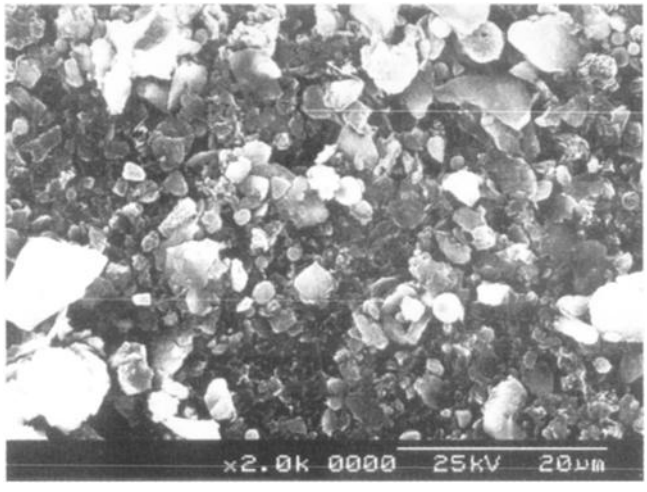

Figure 7. Scanning electron microscope (SEM) photographs of snow impurities collected on Nuclepore filters for the snow samples (top) 980223A1 (0–5 cm) and (bottom) 980223A2 (5–10 cm) on February 23, 1998.

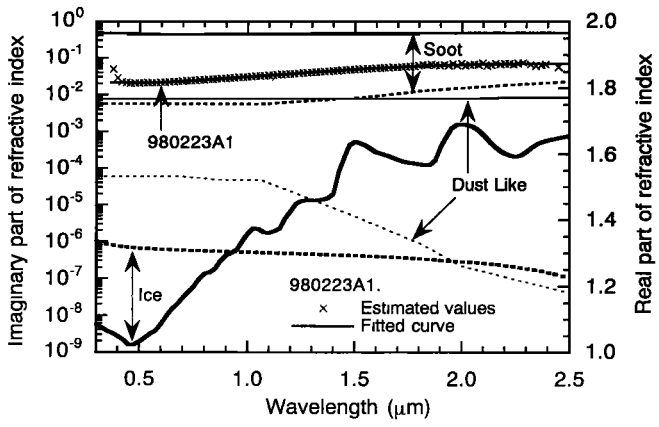

Figure 8. Spectral variations of refractive indices of snow impurities estimated from measurement of the transmittance of a Nuclepore filter on which the impurities in the snow sample 980223A1 had been collected. Imaginary parts ($m_{im}(\lambda)$) are shown by solid lines with the left-hand ordinate, and real parts ($m_{re}(\lambda)$) are shown by dashed lines with the right-hand ordinate. Values for soot [*AFGL*, 1985], dust-like aerosol [*AFGL*, 1985], and ice [*Warren*, 1984; *Kou et al.*, 1993] are also plotted for comparison. The fitted curve of $m_{im}(\lambda)$ obtained by means of a cubic equation of wavelength for the snow sample is given by $m_{im}(\lambda) = -0.0141\lambda^3 + 0.0611\lambda^2 - 0.0478\lambda + 0.0317$.

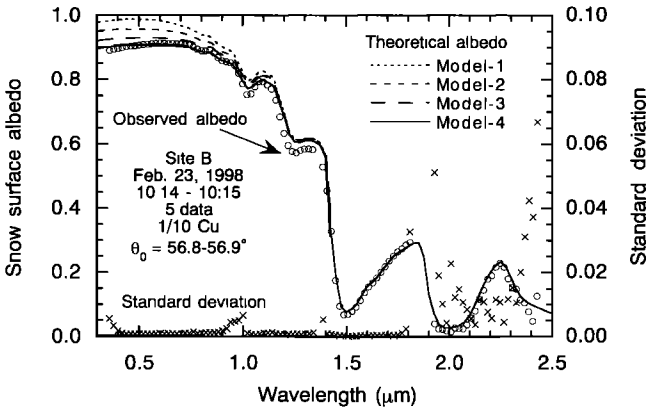

Figure 9. Observed spectral albedo (left-hand ordinate), its standard deviation (right ordinate) on February 23, 1998, and theoretically calculated spectral albedos for four kinds of snow models shown in Figure 10. Observed data are thinned down to one twentieth and only those for which the standard deviation was less than 0.1 are shown. Other observation conditions are shown in Table 1.

snow impurities reviewed by *Warren and Wiscombe* [1980] and for dust-like aerosol compiled by *AFGL* [1985]. This may owe to three possible reasons: (1) the overestimation of $\beta_a(\lambda)$ due to the multiple scattering by the overlapped particles of impurities, (2) the overestimation of $\beta_a(\lambda)$ due to the internal reflection in the Nuclepore filter as described by *Clarke* [1982], and (3) the containing of soot in our samples as mentioned in the first paragraph of this section. Since the effect of the second reason is evaluated to be as much as 30% [*Clarke*, 1982], the first or the third one could be the main reason. Since the measured values of $m_{im}(\lambda)$ were scattered in the regions of $\lambda < 0.4$ μm and $\lambda > 1.8$ μm due to low SNR (see Figure 8), the fitted curve of $m_{im}(\lambda)$ obtained by means of a cubic equation of wavelength was used in calculation of the spectral albedo of the snow surface. We obtained the curves of $m_{im}(\lambda)$ for all of our samples. On the other hand, the real part of the refractive index, $m_{re}(\lambda)$, is generally measured by the immersion oil technique [*Patterson et al.*, 1977], in which the sample is immersed in an oil whose indices of refraction and dispersion are known. This technique also makes the sample unsuitable for the use in SEM analysis after the measurement. We therefore assumed the value of $m_{re}(\lambda)$ for dust-like aerosol compiled by *AFGL* [1985] as shown on the right-hand scale in Figure 8.

6. Effects of Snow Physical Parameters on Spectral Albedo

6.1. Snow Layer Structure

The spectral albedo observed on February 23 was compared with the theoretical values, as shown in Figure 9, where the observed and theoretical spectral albedos are shown on the left-hand scale, and the standard deviation of observed albedo is on the right-hand scale. At the wavelengths where a large standard deviation was observed, the energy of the downward solar flux was relatively weak compared with the sensitivity of the detector of our spectrometer. This is due mainly to the low sensitivity of the detector itself ($\lambda \sim 0.95$ μm and $\lambda > 1.8$ μm), and the energy of the downward solar flux was low because of the atmospheric absorption bands ($\lambda \sim 0.4$, 1.4, 1.9, and 2.5 μm). Except for these wavelengths, low values of standard deviation less than 0.005 were obtained. The theoretical spectral albedos were calculated for four kinds of snow models (Figure 10), in which layer thickness, effective snow grain radius (r_{eff}), and the concentration of impurities (s) were varied.

Model 1 consists of a pure snow layer with $r_{eff} = 55$ μm and a semi-infinite snow depth. The grain size was determined from a comparison between the observed spectral albedo and the theoretical one in the region of $\lambda > 1.4$ μm. This was based on the theoretical calculation by *Warren and Wiscombe* [1980], in which there are no significant effects of impurities on spectral albedo in this wavelength region because of the high value of $m_{im}(\lambda)$ for the ice and its much larger volume fraction compared with the impurities. The theoretical albedo agrees with the observed one very well in this wavelength region. The value of $r_{eff} = 55$ μm agrees with r_2 better than r_1, where r_1 is one-half the length of the major axis of crystals or dendrites, and r_2 is one-half the branch width of dendrites or one-half the dimension of the narrower portion of broken crystals as shown in Figure 2. The relation between the near-infrared albedo and snow grain size will be further discussed in section 6.3. In the region of $\lambda < 1.4$ μm the observed albedo is lower than the theoretical one. Some situations in parameters such as total snow depth and vertical profiles of snow grain size and impurities could be considered as the reasons for this discrepancy between the albedos. To examine this, the observed albedo was

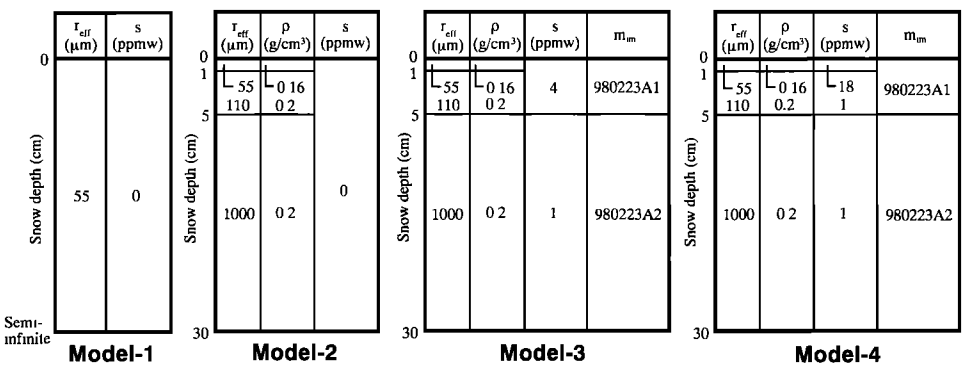

Figure 10. Snow models for which the theoretical spectral albedos were compared with the measurement on February 23, 1998, where r_{eff} is the effective snow grain radius, ρ is the snow density, and s is the concentration of impurities. In the column of m_{im} the name of the snow sample is indicated from which the imaginary refractive index of impurities was derived.

compared with the theoretical one calculated for Model 2 without impurities, in which the snow grain size, depth, and density were determined from the results of snow pit work. The observed snow grain size (particularly r_2) varies drastically near the surface (see Figure 2b). To simulate this condition, in Model 2 we assumed three pure layers with $r_{eff} = 55$ μm (0–1 cm), 110 μm (1–5 cm), and 1000 μm (5–30 cm). In the second layer the value of $r_{eff} = 110$ μm was assumed to be twice that of $r_{eff} = 55$ μm in the top layer according to the measurements of r_2. For snow density the observed value $\rho = 0.16$ g/cm^3 was assumed for the top layer and a constant value $\rho = 0.2$ g/cm^3 was assumed for the two lower layers. The visible albedo is reduced in Model 2 but is not sufficiently low. This is due to the snow impurities, as we have mentioned above. The measured concentration of impurities was 4.0 ppmw in the layer of 0–5 cm and 1.2 ppmw in the layer of 5–10 cm. We made Model 3, which was the same as Model 2 except for the impurities whose concentration was assumed to be $s = 4$ ppmw for the top two layers and $s = 1$ ppmw for the bottom layer. The theoretical albedo for Model 3 is further reduced in the region of $\lambda < 1.0$ μm but does not yet correspond to the observed one. Now we considered that the snow impurities might have been concentrated at the surface, and Model 4 was made in which the concentration of impurities was assumed to be $s = 18$ ppmw for the top 0- to 1-cm layer and $s = 1$ ppmw for the two lower layers. The concentration in the top layer was set to keep the total column amount of impurities in the layers of 0–5 cm as determined from the observed value of 3.6 μg/cm^2, where it was 3.7 μg/cm^2 for Model 4. We can see the best agreement between the observed albedo and the theoretical one with Model 4. These results suggest that only a thin top layer rather than the whole depth of 0–5 cm of snow was highly contaminated, and this occurred due to dry fallout of atmospheric aerosols. This conclusion holds even if the values of the absorption coefficients of impurities were overestimated due to multiple scattering by the particles of impurities as mentioned in section 5.2. A small discrepancy in the albedo between observed and calculated values is noted only in the region of $1.2 < \lambda < 1.4$ μm. Similar results were also found from the data of the other days as will be shown in section 6.2, although the reason is not clear at this stage.

6.2. Estimation of Snow Impurities

Theoretical calculations of spectral albedo using snow models similar to Model 4 were performed for February 22, 24, and 25 and compared with the observations as shown in Figures 11a–11c. The snow models assumed for these three days are shown in Figures 12a–12c, respectively. The effective grain radius (r_{eff}) and snow density (ρ) were determined by the same method as in the previous section 6.1. In the case of February 22 the best agreement is obtained using the value of s close to the measurement. However, on February 24 the value of s by which the theoretical albedo agrees with the observed one is 50 ppmw in the layer of 0–0.5 cm. In this case the total column amount of impurities in the layer of 0–5 cm is 5.7 μg/cm^2, which is somewhat larger than the measured value (4.1 μg/cm^2). This result may be due to an error in the thickness of snow sampling because it is not easy to take a snow sample of the layer of 0–5 cm precisely. In the case of February 25 a good agreement is obtained for $s = 20$ ppmw with a total column amount of impurities 5.8 μg/cm^2, in the layer of 0–5 cm (the measured value was 6.0 μg/cm^2). From these analyses we can delineate the daily change in snow contamination as follows:

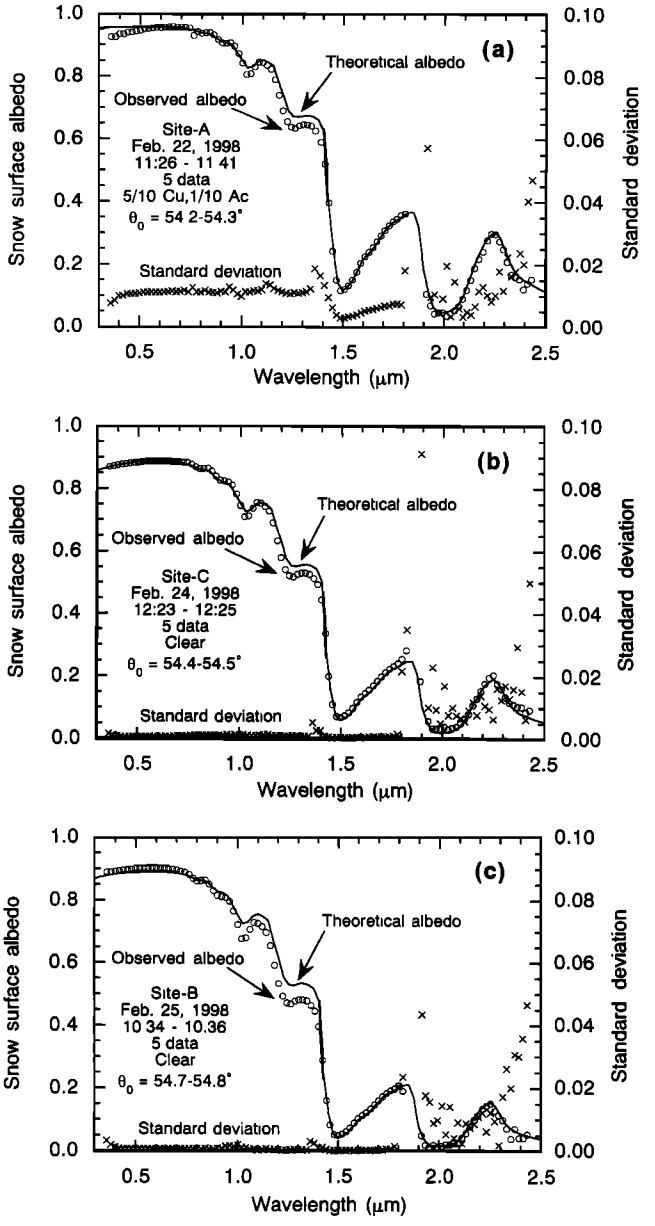

Figure 11. Same as Figure 9 for Model 4 but for (a) February 22, (b) February 24, and (c) February 25 in 1998. Observation conditions are shown in Table 1.

On February 22 just after the snowfalls (February 20 and 21), the snow surface was comparatively clean and had a high visible albedo. Thereafter, snow impurities gradually became concentrated at the surface due to dry fallout of atmospheric aerosols. The measured concentrations of snow impurities in the layers below a 5-cm depth on February 22 were higher than those on the other days. Possible reasons are the difference in observation sites or an error in the thickness of snow sampling. However, even if the value of $s = 1$ ppmw is assumed for the 5–30 cm on February 22, the spectral albedo increases, at maximum, only by 0.001 at $\lambda = 0.5$ μm.

In the above analyses, small discrepancies in albedos between observed and calculated values are still found at around 1.3 μm for all cases in Figures 11a–11c, as was found on February 23. These results suggest that a systematic error in the calculation and/or observation had been present in this

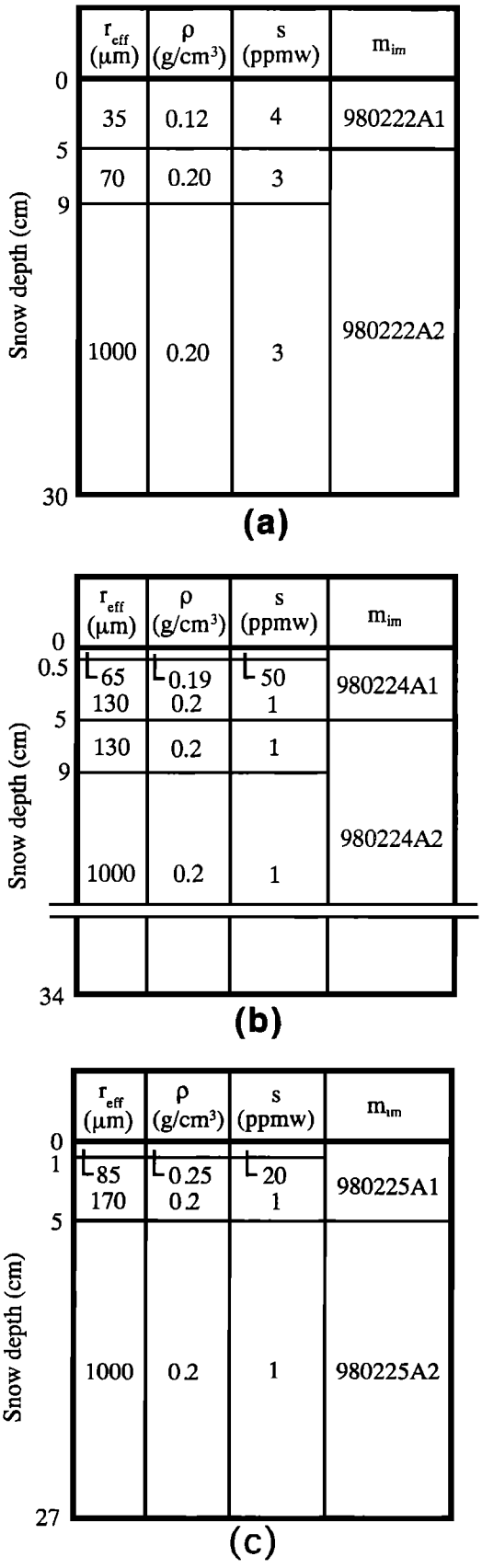

Figure 12. Snow models on (a) February 22, (b) February 24, and (c) February 25, 1998, for which the theoretical spectral albedos were calculated and compared with the measurements as shown in Figure 11.

work, but it has not been clarified at this stage. *Sergent et al.* [1998] discussed that the optical radius (equal to our optically equivalent radius) determined from the measured hemispherical-directional reflectance at $\lambda = 0.99$ μm makes the theoretical value of the spectral hemispherical-directional reflectance agree with the measured one in a wide region of $\lambda = 0.9$–1.45 μm. If such measurement is extended to longer wavelengths, the uncertainty in the present study would be clarified.

6.3. Snow Grain Size

In this section we will compare the optically equivalent snow grain size, which gives the best fit to theoretical spectral albedo, with the in situ measured snow grain size and that determined from micrographs by image processing. *Grenfell et al.* [1981] noted that the observed albedo was lower than that theoretically predicted from the measured snow grain size on the basis of snow pit work, where they defined the snow grain size as 0.5 times the smallest dimension of typical particle. *O'Brien and Koh* [1981] reported that the grain size of new snow theoretically predicted from the near-infrared reflectance was much smaller than that determined on the basis of image processing for replicated ice crystals. *Sergent et al.* [1998] showed that the mean convex radius (defined as the inverse of the mean curvature of the grain contour obtained by the image-analysis system) of snow grains was larger than the optical radius except for large grains, as determined from measurements of hemispherical-directional reflectance at $\lambda = 0.9$–1.45 μm in a cold laboratory. *Aoki et al.* [1998] demonstrated that the optically equivalent grain size is of the order of the branch width of dendrites for new snow. The different relations of observed grain size to model grain size found by these different authors are most likely explained by different choices of equivalent sphere.

We examined in detail the relation between the optically equivalent snow grain size of sphere and the measured geometrical grain size. Table 2 shows the comparison of the grain radii obtained from snow pit work (r_1 and r_2), image processing ($\bar{r}_{image}$ and r^{eff}_{image}), and spectral albedo fitting in the region of $\lambda > 1.4$ μm (r_{fit}). The value of r_1 is the size commonly used in glaciological measurements, with which the values of r_{fit} do not correspond. Most values of r_{fit} are in the range of r_2; that is, the optically equivalent size is of the order of a branch width of dendrites or of a dimension of the narrower portion of broken crystals, just as was found by *Aoki et al.* [1998]. The

Table 2. Comparison of Grain Radii (μm) of Snow Surface Obtained From Snow Pit Work (r_1 and r_2), Image Processing ($\bar{r}_{image}$, r^{eff}_{image} and r_{VA}), and Spectral Albedo Fitting in the Region $\lambda > 1.4$ μm (r_{fit})

1998	r_1	r_2	$\bar{r}_{image}$	r^{eff}_{image}	r_{VA}	r_{fit}
Feb. 22	100–750	50–100	89	140	42	35
Feb. 23	300–500	50–150	109	163	57	55
Feb. 24	100–500	50–150	132	195	77	65
Feb. 25	250–750	50–150	143	220	96	85

Value of r_1 is one-half the length of the major axis of crystals or dendrites, and r_2 is one-half the branch width of dendrites or one-half the dimension of the narrower portion of broken crystals. The values $\bar{r}_{image}$ and r^{eff}_{image} are the mean radius and the effective radius, respectively. The radius of the equal-V/A sphere r_{VA} is given by the equation (12). The value of r_{fit} is a theoretical effective radius of the top layer of snow that gives the best fit to observed spectral albedo in the region of $\lambda > 1.4$ μm.

values of $\bar{r}_{image}$ are 1.6–2.6 times larger than r_{fit}, and the values of r_{image}^{eff} are ~1.5 times larger than $\bar{r}_{image}$. Thus both of the snow grain radii estimated by image processing are not applicable as the optically equivalent grain size to our irregular snow particles. *Grenfell and Warren* [1999] showed that the scattering and absorption properties of a nonspherical ice particle are represented using equal-V/A spheres from the theoretical calculations for a randomly oriented infinite long cylinder of ice. Although we cannot estimate the radius of the equal-V/A sphere accurately for irregular snow grains in our micrographs, we could roughly make an estimate of a radius of the equal-V/A sphere by assuming our snow grains to be hexagonal columns and to lie along the c axis in our micrographs. According to *Grenfell and Warren* [1999] the radius of the equal-V/A sphere r_{VA} for a hexagonal column is given by

$$r_{VA} = \frac{3\sqrt{3}ac}{4c + 2\sqrt{3}a}, \tag{12}$$

where a is the length of each side of the hexagon, and c is the length of the column. The projected area (not a surface area) measured by image processing is $2ac$ and is equal to $\pi\bar{r}_{image}^2$. We here need the ratio $2a/c$, i.e., the width/length ratio of each snow grain. This ratio increases from February 22 to 25 as shown in Figure 3. We roughly estimated the ratios $2a/c$ from our micrographs to be 1/5, 1/4, 1/3, and 1/2, respectively, from February 22 to 25. Thus the values of r_{VA} are obtained as shown in Table 2. These values agree with r_{fit} as discussed by *Grenfell and Warren* [1999].

The grain radius can be defined as the radius of (1) the equal-volume sphere, (2) the equal-surface-area sphere, (3) the equal-projected-area sphere, (4) the equal-V/A sphere, (5) half the long dimension, or (6) half the short dimension. *Grenfell et al.* [1981] and *Aoki et al.* [1998] used definition (6), and the analyses by image processing use definition (3). In general, the snow grain sizes by the definitions, except (4) and (6), are larger than the optically equivalent one. In the paper by *O'Brien and Koh* [1981], very small particles less than 50 μm were not identified as replicated ice crystals, and thus their estimated grain size for new snow as determined by image processing might have been larger than the theoretically predicted one. On the other hand, we confirmed that there was no liquid water in the network of snow grains in our observation. If water exists in the snowpack, it would act to increase the optically equivalent grain size by bonding snow grains.

7. Effects of Snow Physical Parameters on BRDF

7.1. Observation of BRDF

The BRDF observation was carried out on the same snow surface for the albedo measurement on February 25 at Site B of which the results were shown in the previous section 6. This observation was made using two types of optical heads: one was the bare optical fiber whose field of view (FOV) was 25° for full angle and the other was a foreoptics head with 1° FOV attached to the optical fiber. The former was set up as in the case of the albedo observation system (see Figure 5) without WRS, where the azimuth and zenith angles were controlled by turning the azimuth direction of the mount and the viewing direction of the optical fiber arm, respectively. The latter (foreoptics) was set to a goniostage (angle-setting device) on a tripod on the snow surface. Since the distance from the snow surface to the foreoptics was about 1.0 m, even a slight undulation of the snow surface could affect the BRDF pattern observed with the foreoptics, especially at low θ_v. On the contrary, at high θ_v the FOV of the optical fiber was too broad to measure the target accurately. We thus made a composite BRDF pattern from the measurements obtained with the optical fiber for $\theta_v \leq 70°$ and from those obtained with the foreoptics for $\theta_v \geq 80°$.

In the calculation of BRDF it is necessary to measure $F_\lambda(\theta_0)$ as shown in (8). However, it was difficult to obtain its accurate value in measurement with the foreoptics and WRS because the foreoptics head was large in size (60 mm $\phi \times 120$ mm) compared to that of WRS (150 mm $\times$ 150 mm), and it obstructed the light coming from the zenith direction. In many studies involving the BRDF observation the anisotropic reflection factor $R_\lambda(\theta_v, \theta_0, \Delta\phi)$ has been used [*Taylor and Stowe*, 1984a, b; *Brandt et al.*, 1991; *Grenfell et al.*, 1994; *Warren et al.*, 1998] which is defined as

$$R_\lambda(\theta_v, \theta_0, \Delta\phi) = \frac{\pi \mathrm{BRDF}_\lambda(\theta_v, \theta_0, \Delta\phi)}{A_\lambda(\theta_0)}, \tag{13}$$

where $A_\lambda(\theta_0)$ is the spectral albedo. The resulting $R_\lambda(\theta_v, \theta_0, \Delta\phi)$ has an average value of 1.0 over the $(\theta_v, \Delta\phi)$ hemisphere. The value of $R_\lambda(\theta_v, \theta_0, \Delta\phi)$ is expressed only by the upward radiance $I_\lambda(\theta_v, \theta_0, \Delta\phi)$ and is given by

$$R_\lambda(\theta_v, \theta_0, \Delta\phi) = \frac{\pi I_\lambda(\theta_v, \theta_0, \Delta\phi)}{\int_0^{2\pi}\int_0^{\pi/2} I_\lambda(\theta_v, \theta_0, \Delta\phi) \sin\theta\cos\theta \, d\theta \, d(\Delta\phi)}. \tag{14}$$

The merit of using $R_\lambda(\theta_v, \theta_0, \Delta\phi)$ is that it is not necessary to know the value of $F_\lambda(\theta_0)$ in (8). However, the complete angular measurement of $I_\lambda(\theta_v, \theta_0, \Delta\phi)$ is required, and it was not obtained in the case of our observations. We therefore calculated the normalized BRDF (NBRDF) by taking into account the radiance at the nadir. The composite NBRDF pattern was also calculated from each NBRDF obtained by means of the optical fiber and the foreoptics.

Plate 1 shows the observed composite NBRDF for six wavelengths, where we used the display method employed previously by *Taylor and Stowe* [1984a, b] and *Warren et al.* [1998]. The anisotropic reflection property is very significant at λ = 1.64 and 2.21 μm, while in the visible region, the NBRDF patterns are relatively flat. The reason for this was explained by *Leroux et al.* [1999] as follows: since in the visible region the single-scattering albedo is close to unity due to the weak absorption of ice, the BRDF is not influenced by the single-scattering parameter and vice versa in the near-infrared region. A similar result was obtained in the principal plane by *Carlson and Arakelian* [1993] in the measurement of anisotropic reflection in Antarctica. Our result was expected in view of the findings of *Warren et al.* [1998] where the BRDF pattern was found to become more anisotropic with a relatively strong forward peak for $\lambda > 0.9$ μm, where snow is more absorptive. The maximum NBRDF is observed at $\theta_v = 85°$ in the forward scattered direction (the bottom of each map) being 2.2 at λ = 0.52 μm and 16.2 at λ = 1.64 μm. In the side-scattered directions (the left- and right-hand directions on each map), the NBRDF decreases to some degree with the viewing angle in the visible region and increases in the near-infrared region. Observation by ADEOS II/GLI will be made only in the range

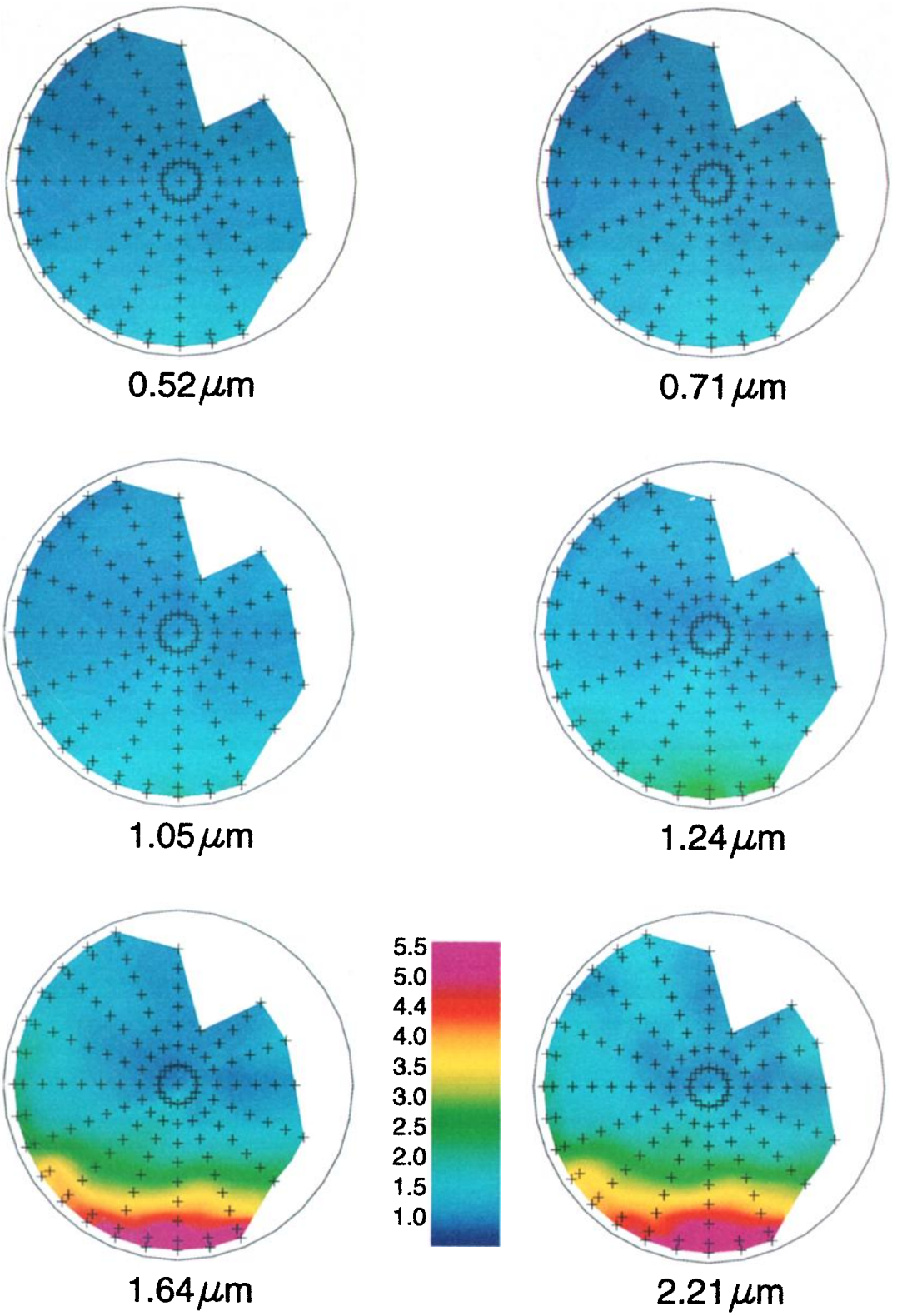

Plate 1. Composite normalized bidirectional reflection distribution function (NBRDFs) of snow for six wavelengths as obtained from measurements of anisotropic reflectance with an optical fiber of 25° field of view (FOV) for $\theta_v \leq 70°$ and those obtained with foreoptics of 1° FOV for $\theta_v \geq 80°$. The measurements using the optical fiber were made in 1222–1258 LT (θ_0 = 54.0°–56.0°) and using the foreoptics in 1320–1334 LT (θ_0 = 57.9°–59.3°) on February 25, 1998, at Site B. All reflectances are normalized by the value at the nadir. The plus signs on each NBRDF map indicate the observed points. The radial coordinate is proportional to the viewing angle θ_v, which is zero at the center of the circle (nadir) and is 90° on the circle. The illumination from the Sun comes from the lower direction of each map, so the bottom of each map is the forward scattering direction.

$\theta_v \leq 45°$, where the NBRDF varies from 0.94 to 1.14 at λ = 0.52 μm and from 0.88 to 2.19 at λ = 1.64 μm. If the appropriate correction on BRDF is not made in the satellite remote sensing, a large amount of error would be present in the retrieved snow parameter values, especially in the near-infrared channels. Furthermore, even the uncertainty of 10% in the snow reflectance at λ = 0.52 μm could bring the serious error for the remote sensing of snow impurities.

7.2. Theoretical Calculation of BRDF and Comparison With Measurement

Plate 2 shows the theoretically calculated patterns of NBRDFs using two different phase functions under the same snow conditions as used in Figure 11c. The first one (left-hand side) was calculated using the single-scattering parameters calculated for spherical ice particles by Mie theory and the second (right-hand side) using the same parameters except for the phase function of Henyey-Greenstein (HG), which was calculated from the same asymmetry factor as in the Mie theory. The most conspicuous difference between these two NBRDFs is the presence of a rainbow in the case of using Mie phase function, where it can be significantly seen at λ = 1.64 μm, and it appears at any wavelength although it cannot be seen clearly. On the other hand, no rainbow is seen at any wavelength in the measurements shown in Plate 1. The second point to be noticed is the maximum value of NBRDF that is seen at just below the horizon in the forward scattering direction. It is higher in NBRDF using the Mie phase function than in using the HG phase function: the values of NBRDF at θ_v = 85° are 3.0 (Mie), 2.2 (HG), and 2.2 (observation) for λ = 0.52 μm and are 23.4 (Mie), 14.2 (HG), and 16.2 (observation) for λ = 1.64 μm. From these comparisons of the theoretical NBRDFs with the measured ones, we see that the HG phase function simulates our measurement of NBRDF better than the Mie theory.

Figure 13 shows Mie and HG phase functions of snow grains in the top layer of the snow model used in these NBRDF calculations. The peak at the scattering angle of around 135° in Mie phase function causes the rainbow of BRDF, and the forward scattering peaks in both phase functions are responsible for the maximum value of BRDF. These phenomena can easily be explained where single scattering by snow grains is dominated. Since multiple scattering by snow grains is dominant in the visible region due to the weak absorption of ice, the pattern due to the single scattering is hidden by the multiple scattering. On the contrary, in the near-infrared region, low-order scattering is dominant due to the strong absorption of ice, and this makes the rainbow or maximum value in the forward scattering region in BRDF. As a result, the shape of the phase function affects the BRDF of snow, and thus the snow grain shape also affects the BRDF. From these points of view it seems that the general hexagonal shapes are not suitable for BRDF calculation, and the spherical shape is not suitable either, because the halo is not usually seen on the snow surface itself although it occasionally appears in the Antarctic Plateau [*Warren et al.*, 1998]. The shapes of snow grains are different from each other and change in the course of the aging of snow. Even in cirrus clouds, the halo does not necessarily appear. In measurements with a polar nephelometer by *Gayet et al.* [1998], examining cirrus of irregular shape, a smooth phase function was observed at forward scattering angles.

Studies on single-scattering properties of nonspherical ice particles in clouds can provide us with useful information for our BRDF studies of the snow surface. One suggestive work was done by *Macke et al.* [1996a] who had calculated the phase function for randomized triadic Koch fractals and found that it becomes smooth with increasing distortion. In this case the complicated shape of the ice particles eliminates particular peaks such as the halo or rainbow in the phase function. Smooth phase functions have been obtained in theoretical calculations for ice particles with inclusions of such as air bubbles or soot [*Macke et al.*, 1996b; *Mishchenko and Macke*, 1997], imperfect hexagonal ice crystals [*Hess et al.*, 1998], a randomly oriented oblate spheroid [*Mishchenko and Travis*, 1998], and a plate of hexagonal ice particles [*Leroux et al.*, 1999]. Comparison of the observations with these models is the next coming item of the present study. In addition, it will be necessary to conduct studies on (1) direct measurement of the phase function of snow particles at each stage of snow age and (2) calculation of single scattering for irregular ice particles.

We have seen in this subsection that the shape of the phase function is important for BRDF calculation. It is now worth checking the effect of the phase function on albedo. Figure 14 shows a comparison of theoretical spectral albedos obtained using Mie and HG phase functions for the snow model of February 25. We see that there is almost no difference in spectral albedo between Mie and HG phase functions. This result holds except for the large θ_0. This means that the asymmetry factor is important for albedo, but the detailed shape of the phase function does not affect the albedo. It leads us to safely say that the use of Mie phase function is appropriate for snow albedo calculations. However, the results presented in this subsection indicate that the observation of only the snow albedo is insufficient for the ground truth in satellite remote sensing of snow.

8. Conclusions

Spectral albedo and BRDF observations in the wavelength range from 0.35 to 2.5 μm were made on a flat snowfield in the midlatitude region. From comparisons of the observed spectral albedos and theoretical ones obtained in calculations using a multiple-scattering model for the atmosphere-snow system, the reduction detected in visible albedo could be explained by the high concentration of snow impurities at the surface ($\leq$1 cm), where the total column amount of impurities in the layer of 0–5 cm was as much as that measured in snow pit work. This suggests that the high concentration of impurities at the surface was caused by dry fallout of atmospheric aerosols. The optically equivalent size of snow grains was estimated on the basis of the albedo in the near-infrared region of $\lambda > 1.4$ μm and was found to be of the order of a branch width of dendrites or of a dimension of the narrower portion of broken crystals. This size was smaller than both the mean grain size and the effective grain size obtained from micrographs by image processing. However, if the snow grains on the micrographs were assumed to be hexagonal columns, the radius of equal volume-to-surface-area ratio sphere became close to the optically equivalent snow grain size. These results suggest that careful interpretation of retrieved data will be necessary in satellite remote sensing of snow grain size and impurities in the future.

In the measurement of BRDF the anisotropic reflection patterns were significant in the near-infrared region of $\lambda > 1.4$ μm, while the visible BRDF patterns were relatively flat. Comparisons with the theoretically calculated BRDFs showed that the HG phase function was more suitable than the Mie phase function, while the spectral albedos calculated with both phase

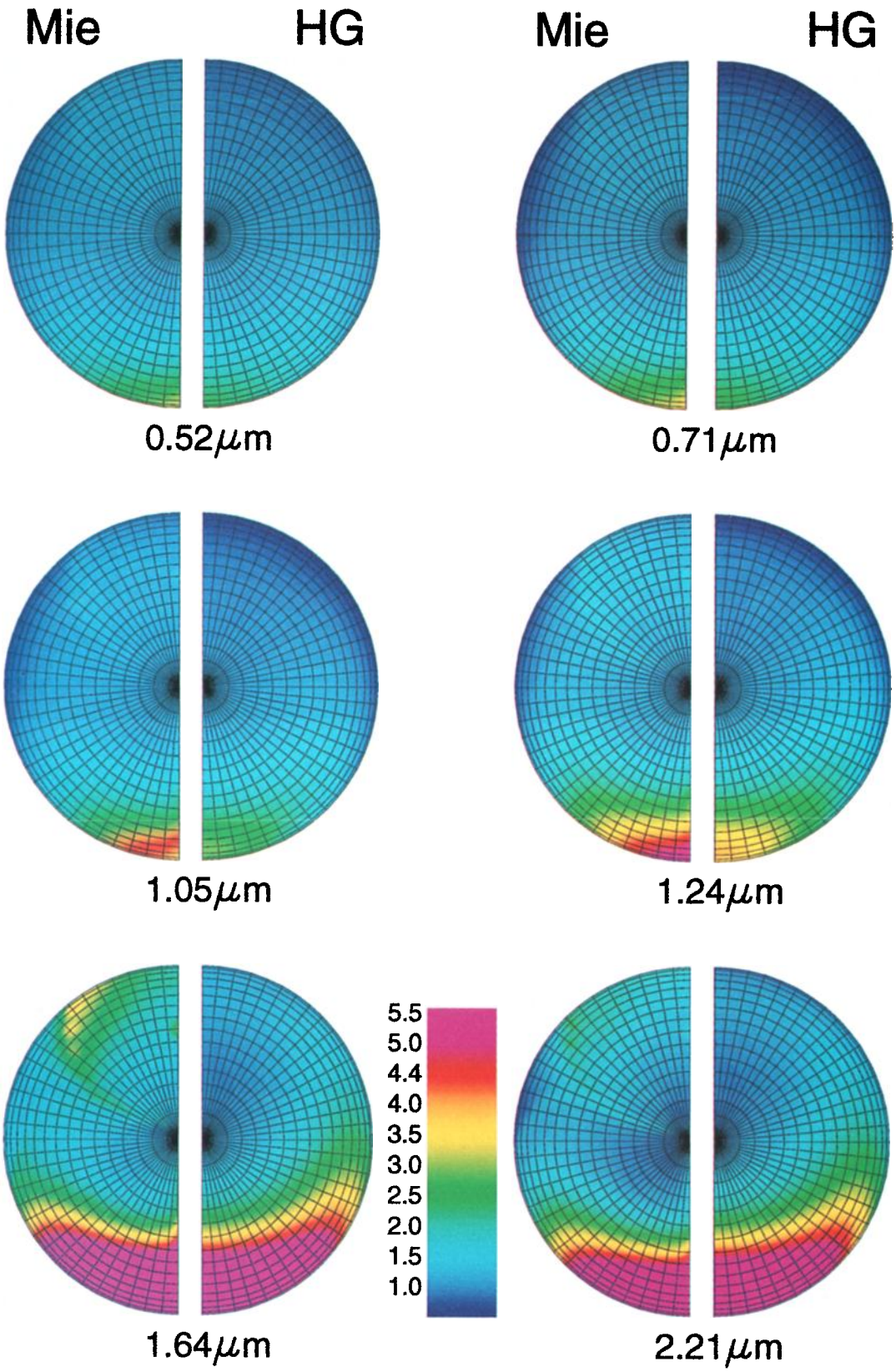

Plate 2. Theoretical NBRDFs of snow for six wavelengths. The semicircular maps on the left-hand side were calculated using Mie phase function and those on the right-hand side using HG phase function. The mesh points on each of the NBRDF maps indicate the grid points where calculations were made.

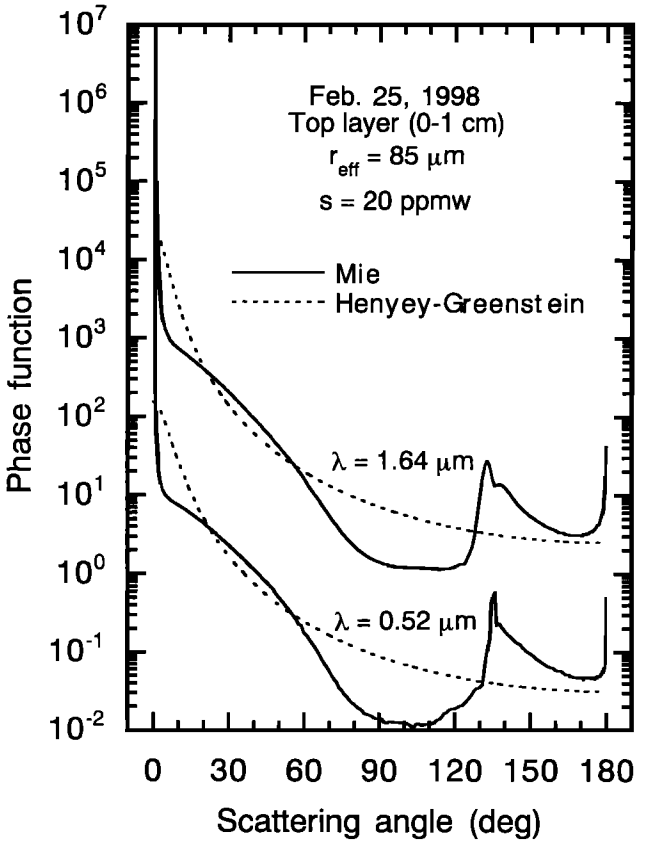

Figure 13. Mie and HG phase functions of snow grains for λ = 0.52 and 1.64 μm in the top layer of the snow model (see Figure 12c) of February 25, 1998. The curves for λ = 1.64 μm are displaced upward by a factor of 10^2.

functions agreed with each other with negligible error. This indicates that the phase function (thus the grain shape) affects the BRDF of snow, and an asymmetry factor is generally important for the spectral albedo. The shapes of individual snow grains are generally so different that a particular shape such as a sphere is not employable for BRDF calculation. It is thus desirable to pursue studies such as the direct measurements of the phase function of snow grains at each stage of the aging of snow together with theoretical calculations for the irregular ice particles. These are important steps required for making a successful satellite remote sensing of snow surface.

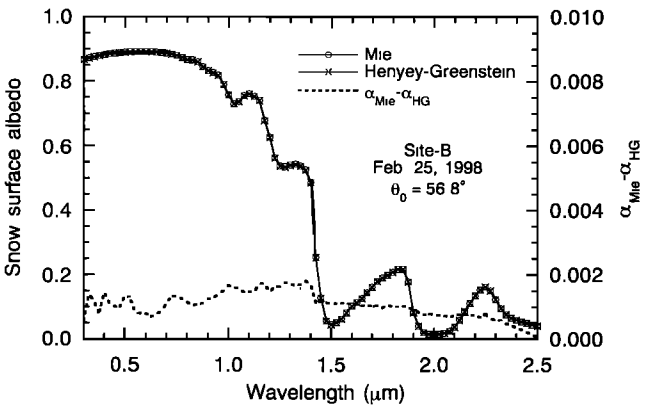

Figure 14. Comparison of theoretical albedos using Mie and HG phase functions (left-hand ordinate) for the snow model of February 25, 1998. The difference between the two albedos is shown on the right-hand ordinate.

Acknowledgments. This work was conducted as part of the ADEOS II/GLI Cal/Val experiment supported by NASDA (National Space Development Agency of Japan). We would like to thank Isao Itoh (Meteorological Research Institute) for developing the albedo observation system. We also thank Yukinori Nakajima, Hiroki Kai, and Yasuhiro Nakajima (Remote Sensing Technology Center) for their logistic support. Thanks are due to Hijiri Himono (Hokkaido University of Education) and Kimiko Shimohara (Kitami Institute of Technology) for their help in this field experiment and to Mineko Yamaguchi (University of Tokyo) and Qingyi Xu (University of Tsukuba) for analyzing the spectral data and collected samples. We are indebted to Kikuo Okada and Masataka Murakami (Meteorological Research Institute), respectively, for the use of the SEM system and the image-processing system. Discussions with Takenori Noumi (Meteorological Collage), Teruyuki Nakajima (University of Tokyo), Takashi Yamanouchi (National Institute of Polar Research), and Harumi Isaka (Université Blaise Pascal) were fruitful for this study.

References

Air Force Geophysics Laboratory (AFGL), *Handbook of Geophysics and the Space Environment*, 1985.

Anderson, G. P., S. A. Clough, F. X. Kneizys, J. H. Chetwynd, and E. P. Shettle, AFGL atmospheric constituent profiles (0–120 km), *Air Force Geophys. Lab. Tech. Rep., AFGL-TR-86-0110*, 43 pp., Air Force Geophys. Lab., Hanscom, Mass., 1986.

Aoki, T., T. Aoki, M. Fukabori, Y. Tachibana, Y. Zaizen, F. Nishio, and T. Oishi, Spectral albedo observation on the snow field at Barrow, Alaska, *Polar Meteorol. Glaciol., 12*, 1–9, 1998.

Aoki, T., T. Aoki, M. Fukabori, and A. Uchiyama, Numerical simulation of the atmospheric effects on snow albedo with a multiple scattering radiative transfer model for the atmosphere-snow system, *J. Meteorol. Soc. Jpn., 77*, 595–614, 1999.

Bohren, C. F., and D. R. Huffman, *Absorption and Scattering of Light by Small Particles*, 530 pp., John Wiley, New York, 1983.

Brandt, R. E., T. C. Grenfell, and S. G. Warren, Optical properties of snow, *Antarct. J. U. S., 26*, 272–275, 1991.

Carlson, R. W, and T. Arakelian, Spectral bidirectional reflectance and energy absorption rates of antarctic snow, *Antarct. J. U. S., 28*, 256–258, 1993.

Chýlek, P., V. Ramaswamy, and V. Srivastava, Albedo of soot-contaminated snow, *J. Geophys. Res., 88*, 10,837–10,843, 1983.

Clarke, A. D., Effects of filter internal reflection coefficient on light absorption measurements made using the integrating plate method, *Appl. Opt., 21*, 3021–3031, 1982.

Dirmhirn, I., and F. D. Eaton, Some characteristics of the albedo of snow, *J. Appl. Meteorol., 14*, 375–379, 1975.

Gayet, J.-F., F. Auriol, S. Oshchepkov, F. Schröder, C. Duroure, G. Febvre, J.-F. Fournol, O. Crépel, P. Personne, and D. Daugereon, In situ measurements of the scattering phase function of stratocumulus, contrails, and cirrus, *Geophys. Res. Lett., 25*, 971–974, 1998.

Grenfell, T. C., A visible and near-infrared scanning photometer for field measurements of spectral albedo and irradiance under polar conditions, *J. Glaciol., 27*, 476–481, 1981.

Grenfell, T. C., and G. A. Maykut, The optical properties of ice and snow in the Arctic Basin, *J. Glaciol., 18*, 445–463, 1977.

Grenfell, T. C., and D. K. Perovich, Spectral albedos of sea ice and incident solar irradiance in the southern Beaufort Sea, *J. Geophys. Res., 89*, 3573–3580, 1984.

Grenfell, T. C., and S. G. Warren, Representation of a nonspherical ice particle by a collection of independent sphere for scattering and absorption of radiation, *J. Geophys. Res., 104*, 31,697–31,709, 1999.

Grenfell, T. C., D. K. Perovich, and J. A. Ogren, Spectral albedos of an alpine snowpack, *Cold Regions Sci. Technol., 4*, 121–127, 1981.

Grenfell, T. C., S. G. Warren, and P. C. Mullen, Reflection of solar radiation by the Antarctic snow surface at ultraviolet, visible, and near-infrared wavelengths, *J. Geophys. Res., 99*, 18,669–18,684, 1994.

Han, W., Remote sensing of surface albedo and cloud properties in the Arctic from AVHRR measurements, 129 pp., D.S. thesis, Univ. of Alaska, Fairbanks, 1996.

Hansen, J. E., Multiple scattering of polarized light in planetary atmospheres, part I, The doubling method, *J. Atmos. Sci.*, *28*, 120–125, 1971.

Hansen, J. E., and L. D. Travis, Light scattering in planetary atmospheres, *Space Sci. Rev.*, *16*, 527–610, 1974.

Hess, M., R. B. A. Koelemeijer, and P. Stammes, Scattering matrices of imperfect hexagonal ice crystals, *J. Quant. Spectrosc. Radiat. Transfer*, *60*, 301–308, 1998.

Japanese National Astronomical Observatory, *Rika Nenpyo* (in Japanese), 1058 pp., Maruzen Co., Ltd., Tokyo, 1999.

Japan Meteorological Agency (JMA), *Annual Report of Background Air Pollution Observation 1997*, 83 pp., Tokyo, 1999.

Kou, L., D. Labrie, and P. Chýlek, Refractive indices of water and ice in the 0.65- to 2.5-μm spectral range, *Appl. Opt.*, *32*, 3531–3540, 1993.

Kuhn, M., Anisotropic reflection from sastrugi fields, *Antarct. J. U. S.*, *9*, 123–125, 1974.

Kuhn, M., Bidirectional reflectance of polar and alpine snow surfaces, *Ann. Glaciol.*, *6*, 164–167, 1985.

Kuhn, M., and L. Siogas, Spectroscopic studies at McMurdo, South Pole, and Siple Stations during the austral summer 1977–78, *Antarct. J. U. S.*, *13*, 178–179, 1978.

Leroux, C., and M. Fily, Modeling the effect of sastrugi on snow reflectance, *J. Geophys. Res.*, *103*, 25,779–25,788, 1998.

Leroux, C., J. Lenoble, J. L. Deuzé, P. Goloub, C. Sergent, and M. Fily, Modeling and measurements of snow reflectance from visible to near infrared, in *IRS'96: Current Problems in Atmospheric Radiation*, edited by W. L. Smith and K. Stamnes, pp. 37–40, 1997.

Leroux, C., J. Lenoble, G. Brogniez, J. W. Hovenier, and J. F. De Haan, A model for the bidirectional polarized reflectance of snow, *J. Quant. Spectrosc. Radiat. Transfer*, *61*, 273–285, 1999.

Li, S., *A model for the anisotropic reflectance of pure snow*, M.S. thesis, 60 pp., Univ. of Calif., Santa Barbara, 1982.

Liljequist, G. H., Energy exchange of an Antarctic snow-field: A, Short-wave radiation; B, Long-wave radiation and radiation balance, in *Norwegian-British-Swedish Antarctic Expedition, 1949–52, Scientific Results*, vol. 2, part 1, 184 pp., Norsk Polarinst., Oslo, 1956.

Lin, C.-I., M. Baker, and R. J. Charlson, Absorption coefficient of atmospheric aerosol: A method for measurement, *Appl. Opt.*, *12*, 1356–1363, 1973.

Lindberg, J. D., and L. S. Laude, Measurement of the absorption coefficient of atmospheric dust, *Appl. Opt.*, *13*, 1923–1927, 1974.

Macke, A., J. Mueller, and E. Raschke, Single scattering properties of atmospheric ice crystals, *J. Atmos. Sci.*, *53*, 2813–2825, 1996a.

Macke, A., M. I. Mishchenko, and B. Cairns, The influence of inclusions on light scattering by large ice particles, *J. Geophys. Res.*, *101*, 23,311–23,316, 1996b.

Mishchenko, M. I., and A. Macke, Asymmetry parameters of the phase function for isolated and densely packed spherical particles with multiple internal inclusions in the geometric optics limit, *J. Quant. Spectrosc. Radiat. Transfer*, *57*, 767–794, 1997.

Mishchenko, M. I., and L. D. Travis, Capabilities and limitations of a current FORTRAN implementation of the T-matrix method for randomly oriented, rotationally symmetric scatterers, *J. Quant. Spectrosc. Radiat. Transfer*, *60*, 309–324, 1998.

Nakajima, T. Y., T. Nakajima, M. Nakajima, H. Fukushima, M. Kuji, A. Uchiyama, and M. Kishino, Optimization of the Advanced Earth Observing Satellite II Global Imager channels by use of radiative transfer calculations, *Appl. Opt.*, *37*, 3149–3163, 1998.

O'Brien, H. W., Observations of the ultraviolet spectral reflectance of snow, *CRREL Rep. 77-27*, U.S. Army Cold Reg. Res. and Eng. Lab., Hanover, N. H., 1977. (Available as *NTIS AD-A046 349/7GI* from Natl. Tech. Inf. Serv., Springfield, Va.)

O'Brien, H. W., and G. Koh, Near-infrared reflectance of snow-covered substrates, *CRREL Rep. 81-21*, U.S. Army Cold Reg. Res. and Eng. Lab., Hanover, N. H., 1981.

O'Brien, H. W., and R. H. Munis, Red and near-infrared spectral reflectance of snow, *CRREL Res. Rep.*, *332*, U.S. Army Cold Reg. Res. and Eng. Lab., Hanover, N. H., 1975. (Available as *NTIS AD-A007 732/1GI* from Natl. Tech. Inf. Serv., Springfield, Va.)

Patterson, E. M., D. A. Gillette, and B. H. Stockton, Complex index of refraction between 300 and 700 nm for Saharan aerosols, *J. Geophys. Res.*, *82*, 3153–3160, 1977.

Salomonson, V. V., and W. E. Marlatt, Anisotropic solar reflectance over white sand, snow and stratus clouds, *J. Appl. Meteorol.*, *7*, 475–483, 1968.

Sergent, C., C. Leroux, E. Pougatch, and F. Guirado, Hemispherical-directional reflectance measurements of natural snow in the 0.9–1.45 μm spectral range: Comparison with adding-doubling modeling, *Ann. Glaciol.*, *26*, 59–63, 1998.

Steffen, K., Bidirectional reflectance of snow at 500–600 nm, in *Large Scale Effects of Seasonal Snow Cover*, edited by B. Goodison et al., 166 pp., *IAHS Publ.*, pp. 415–425, Int. Assoc. of Hydrol. Sci., Wallingford, England, 1987.

Steffen, K., Effect of solar zenith angle on snow anisotropic reflectance, in *IRS'96: Current Problems in Atmospheric Radiation*, ed. by W. L. Smith and K. Stamnes, pp. 41–44, 1997.

Taylor, V. R., and L. L. Stowe, Reflectance characteristics of uniform Earth and cloud surfaces derived from Nimbus 7 ERB, *J. Geophys. Res.*, *89*, 4987–4996, 1984a.

Taylor, V. R., and L. L. Stowe, Atlas of reflectance patterns for uniform earth and cloud surfaces (NIMBUS-7 ERB—61 days), *NOAA Tech Rep. NESDIS 10*, Natl. Oceanic and Atmos. Admin., Washington D. C., 1984b.

Warren, S. G., Optical properties of snow, *Rev. Geophys.*, *20*, 67–89, 1982.

Warren, S. G., Optical constants of ice from the ultraviolet to the microwave, *Appl. Opt.*, *23*, 1206–1225, 1984.

Warren, S. G., and W. J. Wiscombe, A model for the spectral albedo of snow, II, Snow containing atmospheric aerosols, *J. Atmos. Sci.*, *37*, 2734–2745, 1980.

Warren, S. G., T. C. Grenfell, and P. C. Mullen, Optical properties of Antarctic snow, *Antarct. J. U. S.*, *21*, 247–248, 1986.

Warren, S. G., R. E. Brandt, and P. O'Rawe Hinton, Effect of surface roughness on bidirectional reflectance of Antarctic snow, *J. Geophys. Res.*, *103*, 25,789–25,807, 1998.

Wiscombe, W. J., and S. G. Warren, A model for the spectral albedo of snow, I, Pure snow, *J. Atmos. Sci.*, *37*, 2712–2733, 1980.

T. Aoki, T. Aoki, and M. Fukabori, Meteorological Research Institute, 1-1 Nagamine, Tsukuba Ibaraki 305-0052, Japan. (teaoki@mri-jma.go.jp; taaoki@mri-jma.go.jp; fukabori@mri-jma.go.jp)

A. Hachikubo, Kitami Institute of Technology, 165 Koen-cho, Kitami 090-8507, Japan. (hachi@snow2.civil.kitami-it.ac.jp)

F. Nishio, Center for Environmental Remote Sensing, Chiba University, 1-33 Yayoi-cho, Inage-ku, Chiba 263-8522, Japan. (fnishio@ceres.cr.chiba-u.ac.jp)

Y. Tachibana, Research Institute of Civilization, Tokai University, 1117 Kitakaname, Hiratsuka 259-1292, Japan. (tachi@rh.u-tokai.ac.jp)

(Received June 7, 1999; revised November 2, 1999;
accepted November 9, 1999.)